

From breakup to coiling and buckling regimes in buoyant viscoplastic injections

S. Akbari¹ and S.M. Taghavi^{1,†}

¹Department of Chemical Engineering, Université Laval, Québec, QC G1V 0A6, Canada

(Received 17 July 2021; revised 5 February 2022; accepted 16 March 2022)

We study the injection flow of a heavy viscoplastic fluid into a light Newtonian fluid, via modelling and experiments. The injection is carried out downward, via an eccentric inner pipe inside a vertical closed-end outer pipe. This configuration results in a core viscoplastic fluid surrounded by an annular Newtonian fluid. The flow is structured and mixing is negligible. As the injection rate increases in a typical experiment, we observe three distinct flow regimes, associated with the core fluid behaviour, namely the breakup, coiling and buckling (bulging) regimes. In the breakup regime, the core fluid is yielded due to the extension caused by buoyancy, while in the buckling regime the yielding occurs due to the compression promoted by the pressure and the interfacial shear stress applied by the upward flow of the annular fluid. For the coiling regime, the core fluid remains largely unyielded until it exhibits a coiling behaviour. We develop a lubrication approximation model, using the Herschel–Bulkley constitutive equation, with dimensionless flow parameters including the Bingham number, the power-law index, the buoyancy number, the viscosity ratio, the diameter ratio, the eccentricity and the aspect ratio. Based on a reasonable prediction to the yielding onset, the model allows us to classify the flow regimes versus an elegant combination of the dimensionless numbers.

Key words: plastic materials, lubrication theory, core-annular flow

1. Introduction

The injection of a viscoplastic fluid into another fluid occurs in many industrial applications, such as the plug and abandonment (P&A) of oil and gas wells (Nelson & Guillot 2006; Khalifeh & Saasen 2020; Akbari & Taghavi 2021), three-dimensional printing (Karyappa, Ohno & Hashimoto 2019; Lawson *et al.* 2021), etc. From a fluid mechanics perspective, analysing viscoplastic fluid injection processes comes down to quantifying the interface evolution between the fluids, in particular in terms of the yielding

† Email address for correspondence: Seyed-Mohammad.Taghavi@gch.ulaval.ca

behaviour of the viscoplastic fluid (Bonn *et al.* 2017; Frigaard 2019). However, the flow analysis may be complex, due to the presence of a large number of flow parameters, e.g. the density and viscosity ratios, the flow geometry characteristics and the yield stress, resulting in a variety of flow patterns, e.g. breakup, coiling, dripping and buckling of viscoplastic fluids (Balmforth, Frigaard & Ovarlez 2014).

Previous works have mainly considered the dynamics of a viscoplastic fluid injected/extruded under gravity into a dynamically passive exterior fluid, i.e. typically air. In this context, a dynamically passive fluid represents an exterior fluid that is assumed to remain stagnant or whose flow is assumed not to affect the injected fluid flow; in fact, only the exterior fluid's physical properties (e.g. the surface tension with the injected fluid) may affect the injected fluid flow dynamics. On the other hand, a dynamically active fluid, which is in direct contact with the injected fluid at the interface, describes a medium whose flow accompanied by its physical properties exerts significant forces on the injected fluid and, consequently, alters the flow dynamics. For example, Coussot & Gaulard (2005) have experimentally and theoretically investigated the breakup of an extruded viscoplastic fluid into air, finding that an unyielded layer is developed until its weight becomes larger than the yield stress force; this leads to the yielding and breakup of the layer, forming a droplet, the volume of which increases with increasing flow rate. Similar results have been obtained by Al Khatib & Wilson (2005). Surface tension effects have been ignored in these studies, due to high viscosities of the viscoplastic materials considered. Similar observations have been made by Balmforth, Dubash & Slim (2010*a,b*) who have developed a rigorous asymptotic model for the extrusion of a viscoplastic fluid from a nozzle into air, while considering surface tension effects and focusing on the inertialess and inertial extensional dynamics of the resulting viscoplastic filament. They have demonstrated how the yielding of the viscoplastic fluid and the subsequent thinning and progression to pinch-off are governed by rheological, surface tension and gravitational forces. In a relevant work, German & Bertola (2010) have experimentally looked into the slow dripping of a viscoplastic fluid from a thin capillary and qualitatively identified the yield stress effects on the viscoplastic drop stability and the subsequent breakup. Aytouna *et al.* (2013) have analysed the breakup phenomenon in viscoplastic fluid droplets, finding that the pinch-off dynamics in their viscoplastic fluids is similar to that in Newtonian fluids. Zhang *et al.* (2018) have experimentally investigated the yielding of soft-jammed viscoplastic fluids in elongation, suggesting that, to properly analyse the flow dynamics, appropriate constitutive models for yielding and slow-flow regimes need to be developed. Recently, Valette *et al.* (2019) have numerically studied the deformation and breakup dynamics of stretched yield stress filaments. They have observed the appearance of a conical meniscus prior to breakup (as a consequence of yield stress effects) and hemispherical end drops (as a result of capillary effects). The presence of these interface shapes in their observations is indicative of the competition between capillary and yield stress forces. There are, of course, numerous other works on the breakup phenomena in non-Newtonian fluids, but these have mainly considered elastic and viscoelastic fluids (see, for example, Anna & McKinley (2001) as a classical work and Chan *et al.* (2021) as a recent one); therefore, these fall out of the scope of our interest.

When an injected/extruded fluid filament front reaches a solid surface before breaking up, it lies on the surface and starts coiling; this is a well-known feature that has been most rigorously studied for Newtonian fluids by Ribe (2004), e.g. via developing rod-type models considering the stretching, bending and twisting of the viscous filament. For a Newtonian fluid, four distinct coiling regimes (i.e. viscous, gravitational, inertia-gravitational and inertial) have been found, depending on the viscosity, the falling

height and the flow rate (Habibi *et al.* 2006; Ribe, Habibi & Bonn 2012; Habibi *et al.* 2014; Ribe 2017). In the absence of a yield stress, the coiling of power-law fluids has been examined by Pereira, Hachem & Valette (2020) using direct numerical simulations and providing scaling laws. They have observed that both the coil radius and the coiling frequency are a function of the Reynolds number and the power-law index, when viscous and inertial stresses are balanced in the coil. For a viscoplastic fluid, while the gravitational and viscous regimes have been found, the inertial regime has not been observed due to the breakup of the viscoplastic filaments at large falling heights or instabilities at high flow rates (Rahmani *et al.* 2011).

When the axial compression of a straight viscoplastic filament exceeds a critical value, its deformation from the straight configuration, called the buckling phenomenon, can be observed (Balmforth & Hewitt 2013; O'Bryan *et al.* 2021). For example, Rasschaert *et al.* (2018) have experimentally studied the filling of a container by a viscoplastic fluid and characterized dripping, buckling, mounding, planar filling and air entrainment regimes. However, they have found that, at high inertia, the transitions between these patterns are less dependent on the rheological properties of the viscoplastic fluid. There are also a few works on the buckling of pseudoplastic fluids under compression stresses (Pereira *et al.* 2019), identifying capillary and compressive viscous regimes. For such pseudoplastic (shear-thinning) fluids, the effective viscosity decreases with increasing shear rate, but these fluids do not possess a yield stress. In general, the literature of buckling of viscoplastic fluids is not well developed. In fact, despite substantial studies regarding various buckling-associated patterns in viscous or viscoelastic fluid flows, e.g. folding (Ribe 2003; Pan, Phani & Green 2020), bending (Ribe 2001; Teichman & Mahadevan 2003; Tian *et al.* 2020), twisting (Charles, Gazzola & Mahadevan 2019; Wisinger, Maynard & Barone 2019), deflecting (Brun *et al.* 2015), etc., many aspects and patterns in the buckling problem of viscoplastic fluids remain obscure.

In order to better position our study with regard to the developed knowledge in previous works, it may be necessary to further clarify feature classifications for the case of a viscoplastic fluid injected vertically into air (i.e. a dynamically inactive fluid). For such a flow, the main parameters are the yield stress and gravity (and to a lesser extent the surface tension depending on the scale/configuration). For a continuous injection, while the latter (gravity) attempts to yield the viscoplastic fluid, the former (yield stress) resists the yielding. In a downward injection, as the length of the viscoplastic fluid increases, at some point, the gravity force (loosely speaking the material weight) starts to dominate the flow and overcome the yield stress force; therefore, the viscoplastic fluid filament (formed by the injection) can yield, thin and eventually break up, as carefully studied by several researchers (Coussot & Gaulard 2005; Balmforth *et al.* 2010*a,b*; Geffraut *et al.* 2021). If the flow domain is vertically bounded, e.g. by a solid surface positioned at some distance with the respect to the injection inlet, the filament front can reach the surface before the breakup occurs, in which case the filament can exhibit various coiling behaviours, as studied and classified by Rahmani *et al.* (2011) in terms of gravitational, viscous and elastic-dominated dynamics. On the other hand, an upward injection creates an upright column of the viscoplastic fluid, which can eventually yield and bend (buckle) as its length exceeds some limit, e.g. as studied by Balmforth & Hewitt (2013). Although the yielding mechanism may be conceptually similar to that in the downward injection (i.e. the material weight overcoming the yield stress), the yielding in the upward direction is eventually manifested via a form of Euler buckling (Balmforth & Hewitt 2013), as the initially vertical filament bends and finally falls sideways. To summarize, the downward injection of a viscoplastic fluid into air presents two main regimes (breakup and coiling)

and no buckling regime, while the upward injection can typically exhibit a specific bending/buckling behaviour.

As mentioned above, several previous works have considered the extrusion of viscoplastic filaments under the force of gravity, for which the surface tension also plays an important role in governing the flow dynamics. In a more general context, a relevant body of work concerns the competition between the capillary stress and the yield stress in viscoplastic extrusions, via considering the spreading of viscoplastic droplets. For instance, Jalaal, Stoeber & Balmforth (2021) have found that, in contrast to a Newtonian droplet, the resulting viscoplastic droplet reaches a final shape when it is spread on a pre-wetted surface. This and a growing number of similar works find interest in design and manufacturing, e.g. in three-dimensional printing (Jalaal 2016) and coatings processes (Zhang *et al.* 2021).

When multiple and multilayer fluids are considered, a relevant research area to viscoplastic injection flows may include viscoplastic displacements. Significant contributions in this area are numerous, including a wide range of studies over the last two decades. Earlier works, such as those of Allouche, Frigaard & Sona (2000), Dimakopoulos & Tsamopoulos (2007) and Freitas, Soares & Thompson (2011), have focused on residual and deposited layers of viscoplastic fluids and more recent works, such as those of Eslami, Frigaard & Taghavi (2017), Taghavi (2018) and Amiri *et al.* (2019), have further analysed the viscoplastic displacement dynamics, e.g. front heights, shapes and speeds. These and many other similar works have used a variety of analytical, computational and experimental techniques, along with various flows geometries (e.g. narrow and wide channels, pipes, annuli, etc.), to throw light on the yield stress effects in the flow development of viscoplastic fluids, various flow patterns and flow regimes. Since it may not be possible to cite all the relevant viscoplastic displacement studies, to have a better perspective, the interested reader can refer to the appealing reviews by Balmforth *et al.* (2014), Coussot (2014) and Frigaard (2019).

In addition to developing a fundamental understanding, the motivation for the current study of buoyant viscoplastic injections comes from the P&A processes of oil and gas wells, which will be a highly active area over the next couple of decades (Trudel *et al.* 2019; Hassanzadeh, Eslami & Taghavi 2021a,b). These processes are carried out to preserve underground water aquifers and atmosphere from the oil and gas migration (Khalifeh & Saasen 2020). For instance in the dump bailing method, which is a widely used P&A process, a heavy viscoplastic cement slurry is injected (via an eccentric inner pipe) into a long circular casing to remove *in situ* light Newtonian fluids (typically water) and seal the wellbore (Nelson & Guillot 2006). We have recently studied in detail such injection flows, albeit for Newtonian fluids (Akbari & Taghavi 2020, 2021), finding highly dispersive flows. However, to realistically analyse industrially relevant flows, structured viscoplastic fluid flows must be considered. Thus, the study of the non-dispersive viscoplastic injection regime has substantial practical applications.

Most of the previous studies on the injection/extrusion of a viscoplastic fluid into another fluid have considered a dynamically passive *in situ* fluid, which in turn significantly limits the range of interesting phenomena that can be observed. In this work, motivated by P&A applications and inspired by our experiments, we develop a lubrication approximation model to study the downward injection of a heavy viscoplastic fluid into a dynamically active light Newtonian fluid filling a long closed-end pipe. Relying on the Herschel–Bulkley (HB) constitutive equation and a proper asymptotic scaling and reduction, our model will allow us to consider both extensional and compressional stresses affecting the viscoplastic fluid and its yielding condition. The model results will

provide reasonable predictions to our novel experimental observations of three distinct flow regimes, i.e. the breakup, coiling and buckling (bulging) regimes, in terms of the viscoplastic fluid behaviour.

The paper is structured as follows. First, § 2 introduces the experimental materials, apparatus and procedure, and our general experimental observations. Then, § 3 provides the model derivation and § 4 presents our modelling results, their comparisons with the experiments and discussions. Finally, § 5 briefly summarizes the main findings.

2. Experiments

In this section, we first describe our experimental materials, apparatus and procedure, and then we briefly explain our general experimental observations of three distinct flow regimes. We use the latter to motivate the development of an appropriate model in the subsequent section.

2.1. Experimental materials, apparatus and procedure

The experiments involve the downward injection of a heavy viscoplastic fluid into a light *in situ* Newtonian one (see figure 1 and table 2 for the flow parameters). Motivated by P&A applications, in general, an eccentric configuration is considered by installing an eccentric inner pipe inside a vertical closed-end outer pipe (although a limited number of concentric experiments are also performed for comparison purposes). The inner pipe is connected to a gear pump (Ismatech 405A) through which the viscoplastic fluid is injected at a precise flow rate. For the Newtonian fluid filling the outer pipe, water–glycerol mixtures are used. For the injected viscoplastic fluid, water–glycerol mixtures with the addition of Carbopol (Carbomer 940, Making Cosmetics Co.) at various concentrations are employed. The preparation of our viscoplastic fluid follows the established methods in the field (Eslami & Taghavi 2017). For visualization purposes, the viscoplastic fluid is dyed with 800 (mg l⁻¹) of ink (Fountain Pen India black ink). The densities are measured using a high-accuracy density meter (Anton Paar DMA 35).

We perform the rheological measurements of our Carbopol solutions using a rheometer (DHR-3, TA Instruments) with a parallel-plate geometry, with a diameter of 40 (mm) and mean gap of 1 (mm). Fine sandpapers (as rough surfaces) are attached to the rheometer plates to eliminate any possible wall-slip effects in the measurements at low shear rates (Habibi *et al.* 2016; Roberts & Barnes 2001). We obtain the steady-state flow curves of our Carbopol solutions in experiments with controlled shear rate ($\hat{\gamma}$), where the samples are sheared in an upward ramp of $10^{-2} < \hat{\gamma} < 10^3$ (s⁻¹), as shown in figure 2(a). The figure shows the rheometry data represented by the symbols. The flow curves (figure 2a) display the characteristics of the materials above the critical stress. At low shear rates, the shear stress plateaus to a finite value corresponding to the yield stress ($\hat{\tau}_y$). In addition to the yield stress, the samples feature shear-thinning behaviours. As shown, the data points can be well fitted with the lines corresponding to the HB model parameters (Jaworski *et al.* 2021). The model, fitted by the experimental data, has three parameters, i.e. the fluid consistency \hat{k} , the yield stress $\hat{\tau}_y$ and the power-law index n , defined as

$$\left. \begin{aligned} \hat{\gamma} &= 0, & |\hat{\tau}| &\leq \hat{\tau}_y, \\ \hat{\tau} &= \hat{\tau}_y + \hat{k}\hat{\gamma}^n, & |\hat{\tau}| &> \hat{\tau}_y. \end{aligned} \right\} \quad (2.1)$$

The rheological parameters of our Carbopol solutions, obtained using the HB model, are given in table 1 for the fluids depicted in figure 2(a). As expected, at smaller (larger)

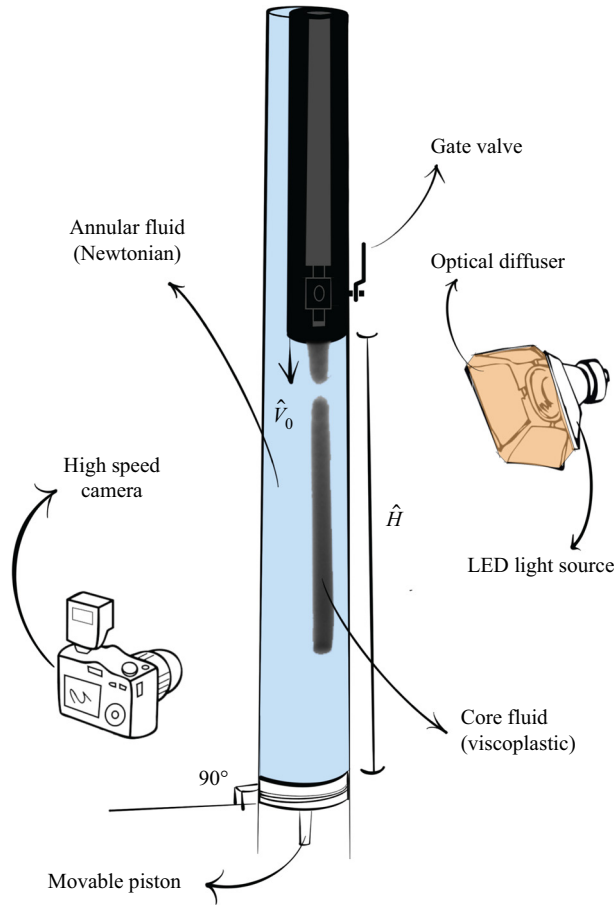


Figure 1. Schematic of the experimental apparatus, wherein a viscoplastic fluid is injected into a vertical closed-end pipe filled with a Newtonian fluid.

Sample	$\hat{\tau}_y$ (Pa)	$\hat{\kappa}$ (Pa s ^{<i>n</i>})	<i>n</i>
I	12.24	30.19	0.260
II	10.25	9.70	0.314
III	6.05	3.02	0.388
IV	4.28	1.56	0.457
V	1.84	0.97	0.481
VI	0.42	0.84	0.532

Table 1. The rheological parameters of Carbopol solutions determined from fitting the shear stress–shear rate curves to the HB model: the yield stress ($\hat{\tau}_y$), the consistency index ($\hat{\kappa}$) and the power-law index (*n*). The Carbopol concentration decreases from Sample I to Sample VI.

Carbopol concentrations, the yield stress values are lower (higher), i.e. the solid-like behaviour of the material is less (more) pronounced, and the required stress to result in yielding is lower (higher).

Although our rheological model choice is the classical HB model, there are also alternative procedures to fit viscoplastic flow curves, e.g. by taking the HB model

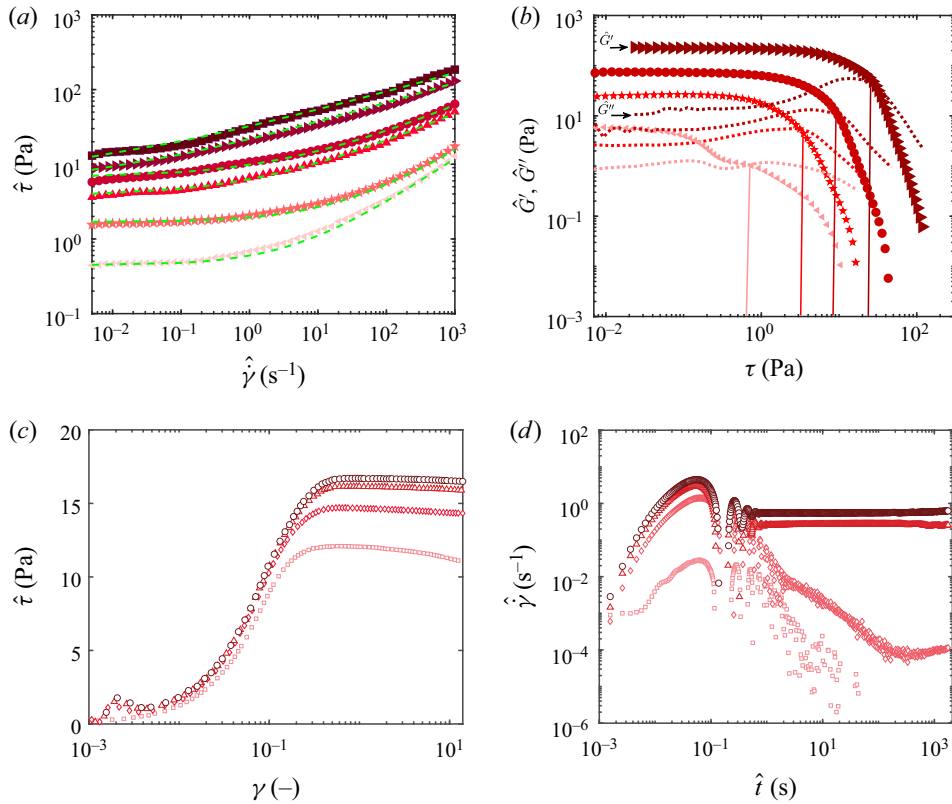


Figure 2. (a) Flow curves of shear stress $\hat{\tau}$ versus shear rate $\hat{\gamma}$ from the shear-rate-controlled tests. The symbols mark Sample I (■), Sample II (►), Sample III (●), Sample IV (▲), Sample V (★) and Sample VI (◄). The green dashed lines correspond to the HB fits, (2.1), with the rheological parameters that are reported for each fluid in table 1. (b) The results of the oscillation amplitude sweep tests for Samples II, III, V and VI. The symbols and dotted lines correspond to the storage (\hat{G}') and loss (\hat{G}'') moduli, respectively. The vertical lines show the intersection of \hat{G}' and \hat{G}'' as an indication of $\hat{\tau}_y$. (c) Shear stress as a function of shear strain at constant shear rates for Sample II at $\hat{\gamma} = 0.0001, 0.001, 0.01$ and 0.1 s^{-1} indicated by square, diamond, triangle and circle symbols, respectively. The scattered data at very low shear strains ($\gamma < 10^{-2}$) are due to instrument artifacts. (d) Creep tests showing shear rate as a function of time for Sample II at $\hat{\tau} = 1, 7, 13$ and 19 Pa , marked by square, diamond, triangle and circle symbols, respectively. The shear rate variations at early times are due to instrument artifacts. Note that, to make the presented data visually distinguishable, the results for some samples are depicted, while the other sample data (not shown) exhibit similar trends. The size and the colour intensity of the symbols represent the following: in (a,b) the Carbopol concentration (i.e. larger and darker symbols represent higher Carbopol concentrations), in (c) the power of the applied shear rate and in (d) the intensity of the applied stress.

as a base. An example is the three-component (TC) model (Caggioni, Trappe & Spicer 2020), defined by $\hat{\tau} = \hat{\tau}_y + \hat{\tau}_y(\hat{\gamma}/\hat{\gamma}_c)^{1/2} + \hat{\eta}_{bg}\hat{\gamma}$, where $\hat{\gamma}_c$ and $\hat{\eta}_{bg}$ are the critical shear rate and the viscosity of the continuous phase, respectively. The TC model represents three regimes of deformation, i.e. the elastic, plastic and viscous regimes. At low shear rates in this model, elastic straining determines the stress and, when the shear rate exceeds a critical value ($\hat{\gamma}_c$), a transition takes place from elastic to plastic. Since the yield stress is an utmost important parameter in our study, we have also used the TC model to extract its value from the rheological data (results omitted for brevity), finding that the yield stresses

Parameter	Name	Range (unit)
\hat{R}_c	Inner radius of inner pipe	6.35 (mm)
\hat{R}	Inner radius of outer pipe	19.05 (mm)
\hat{E}	Eccentricity (radial distance between pipe centres)	0, 6.35 (mm)
\hat{H}	Falling height	20–600 (mm)
\hat{V}_0	Inflow velocity	0.5–675 (mm s ⁻¹)
$\hat{\rho}_c$	Core fluid density	998–1110 (kg m ⁻³)
$\hat{\rho}_a$	Annular fluid density	997–1021 (kg m ⁻³)
$\hat{\mu}_c$	Core fluid viscosity	0.087–430 (Pa s)
$\hat{\mu}_a$	Annular fluid viscosity	0.001–0.025 (Pa s)
$\hat{\tau}_y$	Core fluid yield stress	0.42–12.24 (Pa)
$\hat{\kappa}$	Core fluid consistency index	0.84–30.19 (Pa s ⁿ)
\hat{g}	Gravitational acceleration	9.81 (m s ⁻²)

Table 2. The dimensional parameters and their ranges in our experiments.

obtained by the TC model are on average less than 10 % lower than those fitted by the HB model. Such closeness of yield stress values using these two models has been also reported by Caggioni *et al.* (2020). That said, in this study, we still use the classical HB model, as a simple, common, reliable and accurate model (Frigaard 2019) for describing the rheological behaviours of our Carbopol solutions, in particular the yield stress values.

For the sake of completeness of the rheological characterization, we also perform oscillatory rheometry tests, to characterize elastic and viscous behaviours of our samples at a fixed frequency of 1 (Hz), with applied shear stresses ($\hat{\tau}$) ranging from 0.01 to 200 (Pa). This allows us to evaluate the storage modulus (\hat{G}') and loss modulus (\hat{G}''), which represent the elastic and viscous characteristics, respectively. As shown in figure 2(b), initially (at small $\hat{\tau}$) \hat{G}' is found to be higher than \hat{G}'' for all the sample solutions. This indicates a solid-like behaviour before yielding. For each sample, when the stress exceeds a critical value, an increase in \hat{G}'' accompanied by a decrease in \hat{G}' is observed. Such behaviour has been reported to occur in soft glassy materials (Hyun *et al.* 2011), such as Carbopol gels (Ovarlez, Barral & Coussot 2010). Beyond this critical stress, the viscous response of the material overcomes the elastic one, and both \hat{G}' and \hat{G}'' vary with $\hat{\tau}$. Here, \hat{G}' significantly and \hat{G}'' slightly decrease versus $\hat{\tau}$, in such a way that \hat{G}'' becomes greater than \hat{G}' , indicating that the material is indeed flowing and implying negligible elastic effects. Although the elastic effects of Carbopol solution may be important in certain situations, in this study, we neglect these effects on the flow patterns and dynamics.

The vertical lines in figure 2(b) represent the stress values at which the \hat{G}' and \hat{G}'' curves cross over, implying a rough estimation to the yield stress, as an alternative method (however, note that, as argued by Fernandes *et al.* (2017), estimating the yield point using the crossover must be made with caution). One can also compare these yield stress values with those reported in table 1. The values obtained from the HB model fitting in figure 2(a) are slightly different from the ones computed at the crossover of the \hat{G}' and \hat{G}'' curves. This is in line with recent measurements of similar types of viscoplastic fluids (Dinkgreve *et al.* 2016; Fernandes *et al.* 2017; Jalaal, Kemper & Lohse 2019).

To further complete our rheological characterization, figure 2(c) presents an example of our results in terms of the shear stress as a function of the shear strain for different applied

shear rates. Each curve presents the average of three rheological tests. At low shear strains, the stress curves are close to one another, implying nearly constant properties, regardless of the applied shear rate, hinting at a linear viscoelastic response (Fernandes *et al.* 2017). At higher shear strains, however, the shear stress in each curve rises up as a function of the shear strain, and then deviates from the nearly linear viscoelastic region, to reach a maximum value associated with yielding and rupturing (Bonn *et al.* 2017; Fernandes *et al.* 2017). The maximum shear stress, however, increases with an increase in the applied shear rate value. On the other hand, the yield stress obtained from the shear stress–shear rate flow curve (figure 2*a*, table 1) is slightly lower than the maximum stress at the lowest shear rate in figure 2(*c*) ($\dot{\gamma} = 10^{-4} \text{ (s}^{-1}\text{)}$).

As a final rheological characterization method, figure 2(*d*) presents the results of the creep tests for a given sample, by imposing a constant shear stress and recording the shear rate as a function of time. As seen, for $\hat{\tau} = 1 \text{ (Pa)}$ and $\hat{\tau} = 7 \text{ (Pa)}$, the shear rate approaches zero at long time, implying that the applied stress is lower than the yield stress, i.e. $\hat{\tau}_y = 10.25 \text{ (Pa)}$ evaluated from the shear stress–shear rate flow curve (figure 2*a*, table 1). On the other hand, for $\hat{\tau} = 13 \text{ (Pa)}$ and $\hat{\tau} = 19 \text{ (Pa)}$, the shear rate tends to a constant non-zero value (Espinoza *et al.* 2022), implying that the applied stress is above the yield stress, i.e. an observation generally consistent with the previous measurements.

Note that we consider our experimental pair of fluids (i.e. Carbopol solution and water) to be fully miscible, which means that there are no surface tension effects in our work. This consideration is in line with recent studies demonstrating that the difference between the surface tension of Carbopol solutions and pure water is very small (less than 10%), and this difference does not vary significantly with the Carbopol concentration (Boujlel & Coussot 2013; Jørgensen *et al.* 2015; Jalaal *et al.* 2019).

Before running each experiment, a movable piston is used to adjust the falling height (\hat{H}). Then, the inner and outer pipes are filled with the viscoplastic and Newtonian fluids, respectively, while a gate valve at the inlet initially separates the two fluids. Each experiment begins with opening the gate valve and injecting/extruding the viscoplastic fluid into the Newtonian fluid at a fixed flow rate; simultaneously, the flow images are obtained using a camera (Basler acA2040) at 20 frames per second and transmitted to a computer for subsequent post-processing (via MATLAB). As the injection flow behaviour is expected to be observed below the inlet area, our camera's field of view is focused on this region. A large number of experiments (>300) are performed for different flow rates, falling heights, rheological parameters and density and viscosity ratios.

2.2. Experimental observations of three distinct flow regimes

In this section, we describe the general observations made in our experiments. As mentioned before, our experiments are focused on analysing the viscoplastic fluid flow below the inlet area. For each experiment, the flow rate is chosen and the falling height is fixed. Upon opening the gate valve, which initially separates the fluids, the heavy fluid enters the flow domain below the gate valve and penetrates into the *in situ* light fluid.

Via our experiments, we have identified the following three distinct flow regimes during the injection of the heavy viscoplastic fluid into the light Newtonian fluid (as demonstrated in figure 3):

- (i) *Breakup regime.* A flow example in this regime is illustrated in figure 3(*a*₁). The breakup regime is typically observed at small injection rates (small \hat{V}_0), large buoyancy forces, small to moderate yield stresses of the viscoplastic fluid, small

viscosities of the *in situ* fluid and large falling heights. In this regime, the viscoplastic core fluid is initially extruded as a stable cylinder from the inlet and it advances towards the pipe end. At short times and axial lengths of the core, the stress in the viscoplastic core fluid is below the yield stress, so that a long stable filament can advance downward, holding up against the gravitational forces that attempt to extend it more rapidly. While propagating downward, the core fluid axial length naturally increases and, at a certain point, the core fluid can no longer resist the progressively increasingly buoyancy, which overcomes the yield stress; the core fluid starts to yield and thin near the inlet and it is eventually broken/ruptured. Increasing the buoyancy force (e.g. by increasing the density difference) promotes this flow regime and eases the breakup of the core fluid. After the break of the filament, its upper part which is still connected to the injection inlet is restored fairly rapidly to form a new filament. If the injection continues for a long time in this regime, several filaments can be formed and subsequently break up; the broken parts fall down evenly and make a structure of broken filaments at the bottom end of the pipe.

- (ii) *Coiling regime.* A flow example in this regime is illustrated in [figure 3\(a₂\)](#). The coiling regime is typically observed at moderate injection rates (moderate \hat{V}_0), moderate to large yield stresses of the viscoplastic fluid and relatively short falling heights. In typical situations in this regime, the viscoplastic core fluid is initially extruded, as a stable cylinder, with a diameter that remains typically unchanged as the filament front moves downward. In most cases, the core fluid front can reach the pipe end before the core fluid is broken; then, its front sits on the pipe end and starts coiling evenly, with a fixed centre and a constant coiling frequency (termed regular coiling). As the heavy viscoplastic fluid is injected continuously, the viscoplastic fluid layers are positioned on top of one another, with a thickness initially equal to the nozzle diameter and the coiling of the core fluid gradually continues up to the inlet area. At large velocities, secondary or irregular behaviour (termed irregular coiling) may be observed; at small buoyancy, in some cases the coiling may start to occur before the viscoplastic fluid front reaches the pipe end (termed free coiling). For simplicity, we collectively classify all these as the coiling regime. In general, the coiling behaviour observed in our experiments is reminiscent of the coiling of a viscous fluid filament or an elastic rope falling onto a solid surface, as studied by previous works (Habibi *et al.* 2006; Ribe *et al.* 2012; Ribe 2017), explaining the coiling mechanism via a balance among viscous, gravitational, inertial and elastic stresses.
- (iii) *Buckling regime.* A flow example in this regime is illustrated in [figure 3\(a₃\)](#). The buckling (bulging) regime is typically observed at large injection rates (large \hat{V}_0), small buoyancy forces, low yield stresses of the viscoplastic fluid and high viscosities of the *in situ* fluid. In this regime, as the heavy core fluid penetrates into the *in situ* light fluid, it undergoes axial compressions, due to the pressure gradient and shear stresses at the interface, applied by the resistive upward flow of the annular fluid, resulting in the yielding of the core fluid. As the yield stress is overcome, the core fluid buckles and it quickly expands radially. With time, the radial expansion continues until the injected fluid completely blocks the region near the inlet boundary, and impedes the removal of the light *in situ* fluid from the bottom of the pipe. Increasing the injection velocity and viscosifying the *in situ* fluid promote the viscous compressional stresses towards yielding and buckling of the core fluid. Note that, in the context of our results throughout the text, the buckling regime

concerns a radial expansion and buckling of the viscoplastic core fluid and, therefore, can be also called the bulging regime.

In general, the flow regimes observed and explained above can be also visualized in a concentric flow configuration. To illustrate this, we have conducted a number of experiments in a second apparatus, made of two concentric pipes, for which the results are shown in [figure 3\(b\)](#). As seen, the observed flow regimes in the injection of a viscoplastic fluid into the *in situ* fluid using the concentric inner pipe are similar to the regimes that occur in the eccentric case (compare top and bottom panel groups in [figure 3](#)).

Let us clarify the criterion for classifying our experimental observations into the three defined regimes. To be systematic, this is based on analysing the variation of the viscoplastic filament radius in the upper half of the domain, which renders consistent measurements. To do so, the variation of the ratio between the minimum and maximum radii of the filament, $\hat{R}_{min}/\hat{R}_{max}$, is quantified versus time, as exemplified in [figure 4\(a\)](#). If this ratio ($\hat{R}_{min}/\hat{R}_{max}$) tends to zero at long time, implying that the core fluid is yielded towards breakup, we quantify the flow as the breakup regime. When the core buckles (bulges), $\hat{R}_{min}/\hat{R}_{max}$ tends to a constant value, i.e. $\hat{R}_{min}/\hat{R}_c \approx 1/3$ at long times (marked by the dashed line in [figure 4a](#)). For the experiments in which $\hat{R}_{min}/\hat{R}_{max}$ does not reach zero or the constant value of $\sim 1/3$ at long times (and in fact $\hat{R}_{min}/\hat{R}_{max} \approx 1$), the type of flow regime is classified as the coiling regime. Our classification criterion/approach allows us to circumvent various flow complexities and secondary flow behaviours, e.g. in the coiling regime (which may exhibit regular, free and irregular coiling), providing a simple way to classify our complex flow in terms of the main behaviours.

We have experimentally observed that, in some cases categorized within the coiling regime, as the flow develops the core fluid is actually yielded and starts thinning, while its radius decreases; however, the core fluid front eventually reaches the pipe end before any breakup can occur and starts coiling. A typical example of such a case is presented in [figure 4\(b\)](#). As can be seen, the value of the core radius recovers after the initial decrease. Note that increasing the falling height (H) in such cases would lead to the breakup of the core. However, since the breakup does not actually occur for the used experimental falling height, we still classify these flows as the coiling regime (while highlighting the corresponding results in the results section).

It may be worth mentioning that, in terms of the breakup regime, previous relevant studies (e.g. those considering the injection of a viscoplastic fluid into air) have reported a strong conical shape of the core at the breakup point, which also highly depends on the capillary effects and the core density (Balmforth *et al.* 2010b; Moschopoulos *et al.* 2020; Geffrault *et al.* 2021). However, in our miscible buoyant flow, the surface tension effects are neglected, the density differences are small and the core plasticity is more pronounced, resulting in a relatively more flat shape at the breakup point (e.g. [figure 3a](#)). This may be conceptually in line with the finding of Balmforth *et al.* (2010b) who have shown that, when the yield stress effects dominate the surface tension ones, the breakup point shape changes to a flatter end cone.

Before we proceed, it may be worth mentioning that viscoplastic fluids are known to slip on smooth solid surfaces, for example glass plates (Jalaal, Balmforth & Stoeber 2015) and hydrophobic surfaces (Rahmani & Taghavi 2020). However, in this study, we do not expect the viscoplastic Carbopol flow in the pipe to be influenced by slippage on the surface of the outer pipe, since there is no direct contact between the injected viscoplastic fluid and the outer pipe wall. In fact, in the time scale of our interest, the *in situ* (Newtonian) fluid always exists and separates the injected viscoplastic fluid and

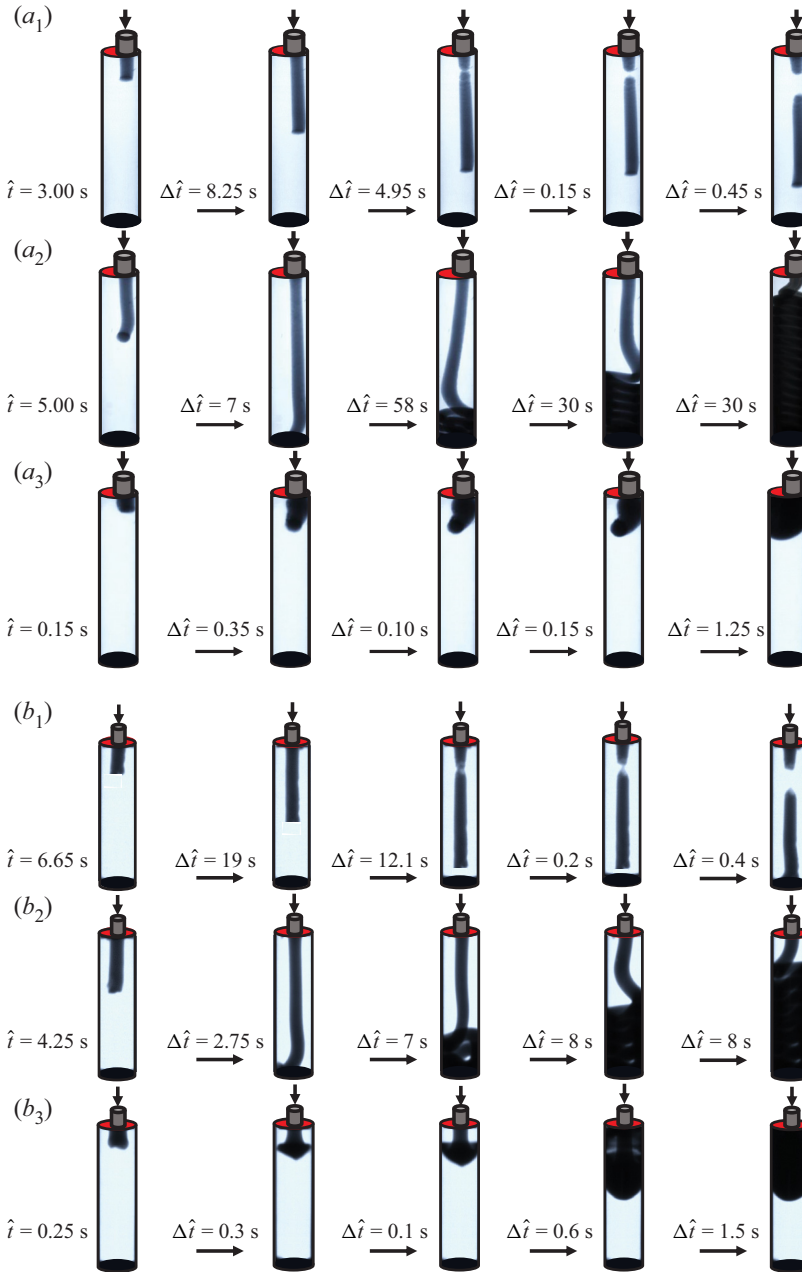


Figure 3. (a) Injection of viscoplastic fluid into closed-end pipe filled with Newtonian fluid through an eccentric inner pipe ($\hat{E} = 6.35$ mm): (a₁) breakup regime for $\hat{V}_0 = 5.3$ mm s⁻¹, $\hat{\rho}_a = 998$ kg m⁻³ and $\hat{\mu}_a = 0.001$ Pa s; (a₂) coiling regime for $\hat{V}_0 = 25.5$ mm s⁻¹, $\hat{\rho}_a = 998$ kg m⁻³ and $\hat{\mu}_a = 0.001$ Pa s; (a₃) buckling (bulging) regime for $\hat{V}_0 = 87.5$ mm s⁻¹, $\hat{\rho}_a = 1007.5$ kg m⁻³ and $\hat{\mu}_a = 0.025$ Pa s. For all the snapshots, $\hat{H} = 200$ mm and the field of view is 20×3.81 cm². (b) Injection through a concentric inner pipe ($\hat{E} = 0$ mm): (b₁) breakup regime for $\hat{V}_0 = 7.3$ mm s⁻¹; (b₂) coiling regime for $\hat{V}_0 = 40.4$ mm s⁻¹; (b₃) buckling (bulging) regime for $\hat{V}_0 = 117.5$ mm s⁻¹. For all the snapshots, $\hat{H} = 100$ mm, $\hat{\rho}_a = 997.5$ kg m⁻³ and $\hat{\mu}_a = 0.001$ Pa s and the field of view is 10×3.81 cm². In all panels, the injection fluid is Sample IV (see table 1), $\Delta \hat{t}$ is the time span between the snapshots, the injection inlet is indicated by an arrow and the outlet area of the flow domain is marked by a red surface.

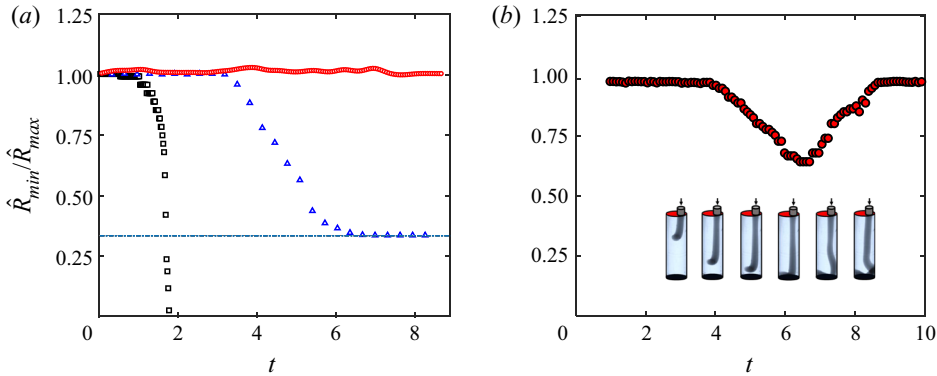


Figure 4. Variation of the core fluid minimum radius identified by $\hat{R}_{min}/\hat{R}_{max}$ versus the dimensionless flow time ($t = \hat{t}\hat{V}_0/\hat{R}$) for Sample V and $\hat{E} = 6.35$ mm. (a) A typical breakup regime (\square) for $\hat{V}_0 = 8.2$ mm s⁻¹, $\hat{\rho}_a = 998$ kg m⁻³, $\hat{\mu}_a = 0.001$ Pa s and $\hat{H} = 400$ mm; a typical coiling regime (\circ) for $\hat{V}_0 = 34.0$ mm s⁻¹, $\hat{\rho}_a = 998$ kg m⁻³, $\hat{\mu}_a = 0.001$ Pa s and $\hat{H} = 400$ mm; a typical buckling regime (Δ) for $\hat{V}_0 = 87.50$ mm s⁻¹, $\hat{\rho}_a = 1007.5$ kg m⁻³, $\hat{\mu}_a = 0.0252$ Pa s and $\hat{H} = 260$ mm. (b) An example of coiling case where the viscoplastic core fluid starts to yield but, due to the finite-sized pipe length, its front reaches the pipe end and it is finally compressed; thus, $\hat{R}_{min}/\hat{R}_{max}$ initially decreases but recovers. The results correspond to $\hat{V}_0 = 34.0$ mm s⁻¹, $\hat{\rho}_a = 998$ kg m⁻³, $\hat{\mu}_a = 0.001$ Pa s, $\hat{H} = 100$ mm and $\hat{E} = 6.35$ mm. The inset shows the initial yielding, the recovering and the eventual coiling of the core fluid, for $t = [3.68 \ 4.91 \ 5.35 \ 5.80 \ 7.84]$ from left to right.

Parameter	Name	Definition	Experimental range
Re	Reynolds number	$(\hat{\rho}_c + \hat{\rho}_a)\hat{V}_0\hat{R}/(2\hat{\mu}_c)$	10^{-4} – 8×10
χ	Buoyancy number	$(\hat{\rho}_c - \hat{\rho}_a)\hat{g}\hat{R}^2/(\hat{\mu}_c\hat{V}_0)$	10^{-5} – 7.5×10
B	Bingham number	$\hat{\tau}_y\hat{R}/(\hat{\mu}_c\hat{V}_0)$	1.3×10^{-1} – 10
n	Power-law index	—	2.6×10^{-1} – 6.2×10^{-1}
M	Viscosity ratio	$\hat{\mu}_a/\hat{\mu}_c$	10^{-6} – 3×10^{-2}
R_c	Radius ratio	\hat{R}_c/\hat{R}	1/3
E	Eccentricity	\hat{E}/\hat{R}	0, 1/3
$\delta \equiv \frac{1}{H}$	Aspect ratio	\hat{R}/\hat{H}	3.2×10^{-2} – 9.5×10^{-1}

Table 3. The key dimensionless parameters and their ranges in this study. Note that, except for the Reynolds number, these flow dimensionless parameters also serve as inputs to the model developed in this study.

the pipe wall. Considering this argument, we do not expect the pipe wall properties to significantly change the experimental observations, e.g. by causing slippage effects.

Based on the experimental observations, it is clear that the development of a multilayer viscoplastic model is appropriate to gain a deeper understanding of our results and provide predictions to the transition between the aforementioned flow regimes; this also allows an analysis of the effects of certain flow parameters (e.g. the eccentricity or the inner pipe radius) that cannot be easily changed in our experiments. Thus, in what follows, we develop such a model, which will include the key governing dimensionless parameters of table 3, to generalize our results.

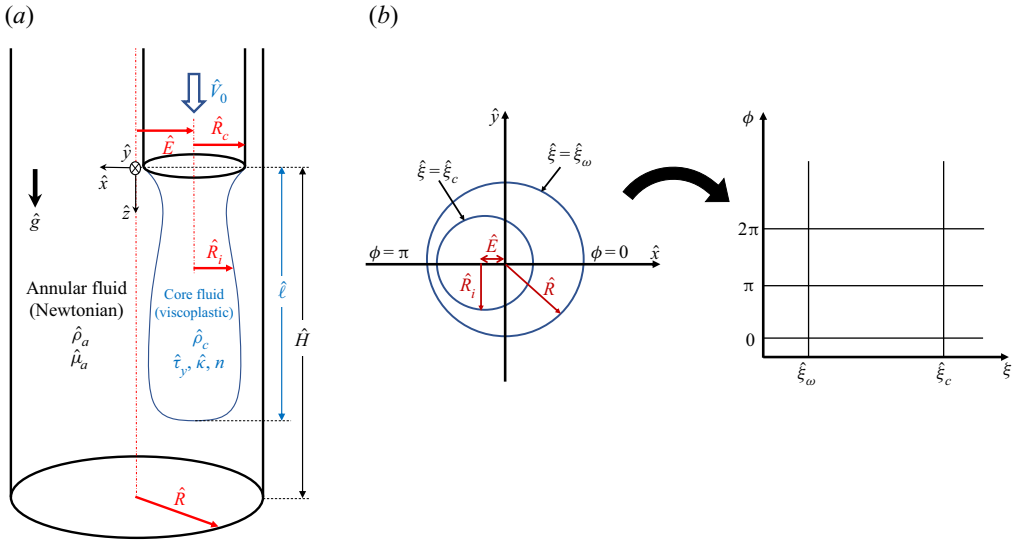


Figure 5. (a) Schematic and flow parameters in our experiments and model. Here, \hat{l} denotes the viscoplastic core length. The \hat{z} axis is aligned with the gravity vector. The subscripts c and a refer to the core and annular fluids, respectively, and the hat symbol is used for dimensional quantities throughout the text. (b) Representation of the conformal mapping of the eccentric flow from Cartesian coordinates to bipolar coordinates.

3. Model formulation

We consider an incompressible viscoplastic core fluid, which follows the HB constitutive model, and an annular fluid, which is Newtonian (see figure 5a for a schematic). Since our problem involves non-coaxial cylinders (eccentric annuli), we use the bipolar coordinates (ξ, ϕ, z) , in which the z axis points vertically downward, in the main direction of the viscoplastic fluid flow. We assume that the pure heavy viscoplastic fluid is injected from the inlet into the light Newtonian fluid, at a mean velocity \hat{V}_0 . To render the equations and parameters dimensionless, we use \hat{V}_0 as the velocity scale, \hat{R} as the length scale, \hat{R}/\hat{V}_0 as the time scale and $\hat{\mu}_c \hat{V}_0/\hat{R}$ to scale pressure and stresses. Here,

$$\hat{\mu}_c = \hat{\kappa} (\hat{V}_0/\hat{R})^{n-1} \tag{3.1}$$

is a characteristic viscosity of the core fluid. Although the two fluids are miscible, we consider the limit in which the Péclet number is large, i.e.

$$Pe = \hat{V}_0 \hat{R}/\hat{D}_m \gg 1, \tag{3.2}$$

where $\hat{D}_m \sim 10^{-9}$ ($\text{m}^2 \text{s}^{-1}$) is the molecular diffusion. This implies that there is no significant mixing occurring over the time scales of our interest.

The model equations are the motion and continuity equations:

$$Re[1 \pm At](\mathbf{u}_t + \mathbf{u} \cdot \nabla \mathbf{u}) = -\nabla p + \nabla \cdot \boldsymbol{\tau} + \chi_k \mathbf{e}_g, \tag{3.3}$$

$$\nabla \cdot \mathbf{u} = 0, \tag{3.4}$$

where $\mathbf{u} = (u_\xi, u_\phi, u_z)$ denotes the velocity, $\boldsymbol{\tau}$ the deviatoric stress and p the pressure. Note that we have already subtracted the static pressure gradient of the annular fluid from the pressure gradient term before scaling. Here, $\mathbf{e}_g = (0, 0, 1)$ and \pm refers to the heavy and

light fluid layers, respectively. In addition, $k = a, c$ refers to the core and annular layers, respectively; also $\chi_a = 0$ and $\chi_c = \chi$ is the buoyancy number, defined as

$$\chi = \frac{(\hat{\rho}_c - \hat{\rho}_a)\hat{g}\hat{R}^2}{\hat{\mu}_c\hat{V}_0}. \tag{3.5}$$

The two fluids are separated by a single interface, for which the surface is defined as

$$F(\xi, \phi, z, t) = \xi - \xi_c = 0, \tag{3.6}$$

in which $\xi_c = \xi_c(z, t)$ is the core fluid interface position and t is time. For $t > 0$, the no-slip boundary conditions are satisfied at the pipe walls represented by $\xi = \xi_w$ and, since the pipe end is closed, outflow conditions are imposed at the eccentric annular space surrounding the injection inlet.

Regarding (3.3), we take the density difference to be small, i.e.

$$At = \frac{\hat{\rho}_c - \hat{\rho}_a}{\hat{\rho}_c + \hat{\rho}_a} \ll 1, \tag{3.7}$$

implying that At , i.e. the Atwood number, is not a governing dimensionless number of the flow.

Regarding the constitutive equations, for the Newtonian annular fluid we simply have

$$\tau_{a,ij} = M\dot{\gamma}_{ij}(\mathbf{u}), \tag{3.8}$$

where M is the viscosity ratio, i.e.

$$M = \frac{\hat{\mu}_a}{\hat{\mu}_c}, \tag{3.9}$$

in which $\hat{\mu}_a$ is the annular fluid's constant viscosity. The core viscoplastic fluid follows the constitutive laws for HB fluids, which includes also the simpler Bingham, power-law and Newtonian models. In dimensional form, the HB fluids are described by three parameters, i.e. the fluid consistency \hat{k} , the yield stress $\hat{\tau}_y$ and the power-law index n . This model in dimensionless form can be written as

$$\left. \begin{aligned} \dot{\gamma}(\mathbf{u}) = 0 &\Leftrightarrow \tau_c(\mathbf{u}) \leq B, \\ \tau_{c,ij}(\mathbf{u}) = \left[\dot{\gamma}^{n-1}(\mathbf{u}) + \frac{B}{\dot{\gamma}(\mathbf{u})} \right] \dot{\gamma}_{ij}(\mathbf{u}) &\Leftrightarrow \tau_c(\mathbf{u}) > B, \end{aligned} \right\} \tag{3.10}$$

where the strain rate tensor has the following components:

$$\dot{\gamma}_{ij}(\mathbf{u}) = \{ \nabla \mathbf{u} + (\nabla \mathbf{u})^\dagger \}_{ij}, \tag{3.11}$$

and the second invariants, $\dot{\gamma}(\mathbf{u})$ and $\tau_c(\mathbf{u})$, are defined by

$$\dot{\gamma}(\mathbf{u}) = \left[\frac{1}{2} \sum_{i,j=1}^3 [\dot{\gamma}_{ij}(\mathbf{u})]^2 \right]^{1/2}, \quad \tau_c(\mathbf{u}) = \left[\frac{1}{2} \sum_{i,j=1}^3 [\tau_{c,ij}(\mathbf{u})]^2 \right]^{1/2}. \tag{3.12a,b}$$

The Bingham number B is defined as

$$B \equiv \frac{\hat{\tau}_y\hat{R}}{\hat{\mu}_c\hat{V}_0}. \tag{3.13}$$

We focus on a flow that has a long, thin aspect ratio, i.e. after an initial time, the viscoplastic flow develops axially over a length scale $\delta^{-1} \gg 1$ (in which δ can be any

arbitrary small aspect ratio). For simplicity, we define the aspect ratio as

$$\delta = \frac{\hat{R}}{\hat{H}} \equiv \frac{1}{H}, \tag{3.14}$$

in which H is the dimensionless pipe height. Relying on lubrication-type assumptions and following standard methods (Leal 2007), we rescale the parameters as follows:

$$\delta z = Z, \quad \delta t = T, \quad \delta p = P, \quad u_\xi = \delta U_\xi, \quad u_\phi = \delta U_\phi, \quad u_z = u_Z. \tag{3.15}$$

Considering the limit of $\delta \rightarrow 0$ (with Re fixed), in the leading order, the motion and continuity equations become

$$O(Re\delta^3) = -\frac{\partial P_k}{\partial \xi} + O(\delta), \tag{3.16}$$

$$O(Re\delta^3) = -\frac{\partial P_k}{\partial \phi} + O(\delta), \tag{3.17}$$

$$O(Re\delta) = -\frac{\partial P_k}{\partial Z} + \frac{1}{\hbar^2} \frac{\partial(\hbar\tau_{k,\xi Z})}{\partial \xi} + \frac{1}{\hbar^2} \frac{\partial(\hbar\tau_{k,\phi Z})}{\partial \phi} + \delta \frac{\partial \tau_{k,ZZ}}{\partial Z} + \chi_k, \tag{3.18}$$

$$0 = \frac{1}{\hbar^2} \frac{\partial(\hbar U_{k,\xi})}{\partial \xi} + \frac{1}{\hbar^2} \frac{\partial(\hbar U_{k,\phi})}{\partial \phi} + \frac{\partial u_{k,Z}}{\partial Z}, \tag{3.19}$$

where \hbar is the scale factor for the bipolar coordinates defined as

$$\hbar = \frac{\sinh \xi_w}{\cosh \xi - \cos \phi}. \tag{3.20}$$

Note that since our problem involves non-coaxial cylinders (forming an eccentric annulus), it is appropriate to use bipolar coordinates. The conformal mapping from Cartesian coordinates to bipolar coordinates is schematically shown in figure 5(b), which allows the eccentric flow to be mapped into a rectangular region. In this orthogonal coordinate system, the two cylindrical boundaries (i.e. the eccentric core interface and the wall) coincide with two coordinate surfaces having constant values of ξ . The other coordinate, ϕ , represents a set of eccentric cylinders whose centres lie on the x axis, which orthogonally intersect the boundaries. In this bipolar coordinate system representing our eccentric core annular flow, the pipe wall is represented by $\xi = \xi_w$, while the interface between the two fluids is $\xi = \xi_c$. Therefore, the flow in the domain of x - y (see figure 5b) is mapped into a semi-infinite strip in the domain of $(\phi$ - $\xi)$ given by

$$\left. \begin{aligned} \text{annular phase: } & \xi_w < \xi \leq \xi_c; \quad 0 \leq \phi \leq 2\pi, \\ \text{core phase: } & \xi_c < \xi \leq \infty; \quad 0 \leq \phi \leq 2\pi, \end{aligned} \right\} \tag{3.21}$$

where

$$\left. \begin{aligned} \xi_c &= \cosh^{-1} \left[\frac{1 - R_i^2 - E^2}{2R_i E} \right], \\ \xi_w &= \cosh^{-1} \left[\frac{1 - R_i^2 + E^2}{2E} \right], \end{aligned} \right\} \tag{3.22}$$

where R_i is the dimensionless radius of the core fluid layer (i.e. the dimensionless interface radius) and E is the dimensionless eccentricity of the core fluid layer. Note that $R_i = R_c$

at the inlet. Finally, providing the relation between the $(x-y)$ Cartesian coordinates and the $(\phi-\xi)$ bipolar coordinates can be useful for result presentation purposes:

$$\left. \begin{aligned} x &= \frac{\sinh \xi_w \sinh \xi}{\cosh \xi - \cos \phi} + 1 - \frac{\sinh^2 \xi_w}{\cosh \xi_w}, \\ y &= \frac{\sinh \xi_w \sin \phi}{\cosh \xi - \cos \phi}. \end{aligned} \right\} \quad (3.23)$$

3.1. Analysis of the viscoplastic core fluid flow

Regarding the Newtonian annular fluid in (3.18) ($k = a$), the term involving $\tau_{a,ZZ}$ is of $O(\delta)$ and can therefore be ignored. However, for the viscoplastic fluid ($k = c$ in (3.18)), the term involving $\tau_{c,ZZ}$ is large and cannot be ignored, as the flow is dominated by the extensional/compressional dynamics. Therefore, in the leading order, the main equation (axial momentum) for the viscoplastic fluid is

$$0 = -\frac{\partial P_c}{\partial Z} + \frac{1}{\hbar^2} \frac{\partial(\hbar\tau_{c,\xi\xi})}{\partial \xi} + \frac{1}{\hbar^2} \frac{\partial(\hbar\tau_{c,\phi Z})}{\partial \phi} + \delta \frac{\partial \tau_{c,ZZ}}{\partial Z} + \chi. \quad (3.24)$$

However, in general $\tau_{c,ZZ}$ (and accordingly the pressure) in the core phase is an unknown function. This situation results from the fact that the stress is indeterminate in the viscoplastic fluid below the yield stress and, therefore, the motion equations are not sufficient to uniquely determine all the stress components, i.e. a complexity that is frequently encountered in similar problems (Balmforth *et al.* 2010a). To overcome this problem, and in the interest of simplicity, we assume that $\tau_{c,\xi\xi} = \tau_{c,\phi\phi}$, which, in the spirit of the regularization of the constitutive equation (Frigaard & Nouar 2005), allows us to use the continuity equation to find

$$\tau_{c,ZZ} = -2\tau_{c,\xi\xi} = -2\tau_{c,\phi\phi}. \quad (3.25)$$

Considering the dominance of $\tau_{c,ZZ}$ also implies that

$$u_{c,Z}(T, \xi, \phi, Z) = u_{c,Z}(T, Z) + O(\delta^2). \quad (3.26)$$

Let us for now assume that the solution to $\tau_{c,ZZ}$ may be found. The yield condition can be obtained in the leading order as

$$\frac{\sqrt{3}}{2} |\tau_{c,ZZ}| + O(\delta) > B. \quad (3.27)$$

The simplified yield condition criterion above is consistent with some previous theoretical approaches for viscoplastic fluid flows downwardly injected in air, such as the work of Balmforth *et al.* (2010b). However, there are more recent works in the literature, such as the works of Moschopoulos *et al.* (2020) and Geffrault *et al.* (2021), emphasizing the importance of including shear components in the analysis, particularly because, in certain cases, the flows of our consideration can lead to yielded conical shapes even in slender filaments. Nevertheless, for the simplicity of our analysis, we assume that such shear component terms are of higher order in δ and can be ignored. To simplify the analysis,

it is straightforward to apply the normal stress balance at the interface (Leal 2007):

$$(\sigma_a \cdot \mathbf{n}) \cdot \mathbf{n} = (\sigma_c \cdot \mathbf{n}) \cdot \mathbf{n}, \tag{3.28}$$

in which σ_a and σ_c are the stress tensors for the annular and core phases and \mathbf{n} is the unit normal vector inward to the surface:

$$\mathbf{n} = \frac{\nabla F}{|\nabla F|} = \frac{(1/\hbar, 0, -\delta\partial\xi_c/\partial Z)}{\sqrt{(1/\hbar)^2 + (\delta\partial\xi_c/\partial Z)^2}}, \tag{3.29}$$

and, in the leading order, we eventually find

$$\left. \begin{aligned} P_c &= P_a - \frac{\delta\tau_{c,ZZ}}{2}, \\ \tau_{c,\xi Z} &= \tau_{a,\xi_c Z} + \frac{3\hbar\delta\tau_{c,ZZ}}{2} \frac{\partial\xi_c}{\partial Z}, \end{aligned} \right\} \tag{3.30}$$

where $\tau_{a,\xi_c Z} = \tau_{a,\xi Z}|_{\xi=\xi_c}$. First of all, note that since in our study both fluids are miscible (at the limit of large Pe), the surface tension effects are neglected in the derivations of the pressure terms above. Also, note that, again, the term involving $\delta\tau_{c,ZZ}$ is large and cannot be removed compared to the shear stress terms. We now integrate the axial momentum over the cross-section of the core fluid ($\xi_c < \xi \leq \infty; 0 \leq \phi \leq 2\pi$), while using the scale factor as well as the stress balance conditions, to find after considerable algebra

$$0 = -R_i^2 \frac{\partial P_a}{\partial Z} - \frac{1}{\pi} \int_0^{2\pi} \hbar\tau_{a,\xi_c Z} d\phi + \frac{3}{2} \delta \frac{\partial(\tau_{c,ZZ} R_i^2)}{\partial Z} + \chi R_i^2, \tag{3.31}$$

using which $\tau_{c,ZZ}$ can be obtained as

$$\tau_{c,ZZ} = \frac{2}{3\delta R_i^2} \int_Z^L \left[-R_i^2 \frac{\partial P_a}{\partial Z} - \frac{1}{\pi} \int_0^{2\pi} \hbar\tau_{a,\xi_c Z} d\phi + \chi R_i^2 \right] dZ, \tag{3.32}$$

in which, for simplicity, we have applied the free-end boundary condition, i.e.

$$\tau_{c,ZZ}(L) = 0. \tag{3.33}$$

Here, $L = L(T)$ is the core layer length, i.e. an unknown of the problem, which must be calculated for an evolving core viscoplastic layer. The first and second terms in the integral above are unknown at this point, as they represent the dynamic of the annular fluid flow; these will be calculated in the next section, but for now let us assume these terms can be obtained.

The second invariant, $\dot{\gamma}(\mathbf{u})$, in the leading order can be eventually found as

$$\left[\frac{1}{2} \sum_{i,j=1}^3 [\dot{\gamma}_{ij}]^2 \right]^{1/2} = \left| \sqrt{3} \delta \frac{\partial u_{c,Z}}{\partial Z} \right| + O(\delta^2). \tag{3.34}$$

Therefore, the HB constitutive model can be simplified to

$$\left. \begin{aligned} \sqrt{3} \left| \frac{\partial u_{c,Z}}{\partial Z} \right| = 0 &\Leftrightarrow \frac{\sqrt{3}}{2} |\tau_{c,ZZ}| \leq B, \\ \frac{\partial u_{c,Z}}{\partial Z} = \frac{\text{sgn}(\tau_{c,ZZ})}{\delta\sqrt{3}} \left(\frac{\sqrt{3}|\tau_{c,ZZ}|}{2} - B \right)^{1/n} &\Leftrightarrow \frac{\sqrt{3}}{2} |\tau_{c,ZZ}| > B. \end{aligned} \right\} \tag{3.35}$$

Thus, the velocity gradient can be written as

$$\frac{\partial u_{c,Z}}{\partial Z} = \frac{\text{sgn}(\tau_{c,ZZ})}{\delta\sqrt{3}} \left[\max \left(\frac{\sqrt{3}|\tau_{c,ZZ}|}{2} - B, 0 \right) \right]^{1/n}. \quad (3.36)$$

Finally, the velocity can then be obtained as

$$u_{c,Z} = \int_0^Z \frac{\text{sgn}(\tau_{c,ZZ})}{\delta\sqrt{3}} \left[\max \left(\frac{\sqrt{3}|\tau_{c,ZZ}|}{2} - B, 0 \right) \right]^{1/n} dZ + u_{c,Z0}, \quad (3.37)$$

in which $u_{c,Z0} = 1$ comes from the injection boundary condition.

In the next subsection, we analyse the Newtonian annular flow dynamics, which in return affects the viscoplastic core fluid flow development, e.g. via imposing a pressure gradient as well as a non-negligible shear stress at the interface (caused by the motion of the annular fluid). This consideration brings the multiphase nature of the flow into the analysis, highlighting that our annular fluid is dynamically active. However, such an analysis would not be relevant for dynamically inactive in-place fluids, e.g. in the simpler case of the injection of a viscoplastic fluid into air, which has been more frequently studied in the literature (Coussot & Gaulard 2005; Balmforth *et al.* 2010a,b; Geffraut *et al.* 2021).

3.2. Analysis of the Newtonian annular flow

Let us move on to analysing the annular flow, needed to calculate the stress in (3.32), starting with the leading-order axial momentum equation for the annular phase:

$$0 = -\frac{\partial P_a}{\partial Z} + \frac{1}{\hbar^2} \frac{\partial(\hbar\tau_{a,\xi Z})}{\partial \xi} + \frac{1}{\hbar^2} \frac{\partial(\hbar\tau_{a,\phi Z})}{\partial \phi}, \quad (3.38)$$

which using the Newtonian constitutive relation is simplified to

$$f_a = \frac{(\cosh \xi - \cos \phi)^2}{\sin^2 \xi_w} \left(\frac{\partial^2 u_{a,Z}}{\partial \xi^2} + \frac{\partial^2 u_{a,Z}}{\partial \phi^2} \right), \quad (3.39)$$

where $f_a = (1/M)(\partial P_a/\partial Z)$. Also, $u_{a,Z}$ is the leading-order solution to the velocity field in the annular phase. Note that the dependence of $u_{a,Z}(T, \xi, \phi, Z)$ on (T, Z) enters only via the interface satisfying the kinematic condition, introduced further below.

Here, we extend the approach proposed by Goldstein, Ullmann & Brauner (2017) to derive our analytical solution for the annular fluid flow in contact with the core viscoplastic fluid, as the inner boundary. Expectedly, the general solution of the equation is made of two solution types, i.e. the particular solution ($u_{ap,Z}$) and the homogeneous solution ($u_{ah,Z}$). The general solution becomes

$$u_{a,Z} = u_{ah,Z} + u_{ap,Z}. \quad (3.40)$$

Considering the form of the motion equations and non-homogeneous terms, following a classical style, we choose the following particular solution:

$$u_{ap,Z} = \frac{f_a \sinh^2 \xi_w \cosh \xi}{2(\cosh \xi - \cos \phi)}. \quad (3.41)$$

Considering the symmetry condition with respect to the pipe centreline, $\phi = 0, 2\pi$, i.e.

$$\left. \frac{\partial u_{ah,Z}(T, \xi, \phi, Z)}{\partial \phi} \right|_{\phi=0,\pi} = 0, \quad (3.42)$$

it is possible to propose the following homogeneous solution in the form of the following Fourier series:

$$u_{ah,Z} = \sum_{m=0}^{\infty} [\alpha_{am} \cosh(m\xi) + \beta_{am} \sinh(m\xi)] \cos m\phi. \tag{3.43}$$

Following the procedure detailed in Appendix A, the solutions to the annular fluid flow velocity and shear stress are derived as

$$u_{a,Z} = \frac{f_a \sinh^2 \xi_w \cosh \xi}{2(\cosh \xi - \cos \phi)} + \alpha_{a00} + \beta_{a00} + \sum_{m=1}^{\infty} [\alpha_{am} \cosh(m\xi) + \beta_{am} \sinh(m\xi)] \cos m\phi, \tag{3.44}$$

$$\begin{aligned} \tau_{a,\xi Z} &= \frac{M}{\hbar} \frac{\partial u_{a,Z}}{\partial \xi} = \frac{M}{\hbar} \left[-\frac{f_a \sinh^2 \xi_w \sinh \xi \cos \phi}{2(\cosh \xi - \cos \phi)^2} \right] \\ &\quad - \frac{M}{\hbar} \frac{1}{\xi_c - \xi_w} \left[\frac{f_a \sinh^2 \xi_w \cosh \xi_c}{2 \sinh \xi_c} - \frac{f_a \sinh \xi_w \cosh \xi_w}{2} - u_{c,Z} \right] \\ &\quad + \frac{M}{\hbar} \sum_{m=1}^{\infty} m [\alpha_{am} \sinh(m\xi) + \beta_{am} \cosh(m\xi)] \cos(m\phi), \end{aligned} \tag{3.45}$$

for which the coefficients are given in Appendix A.

3.3. Solution procedure for interface evolution

The annular and core fluid flux functions can be obtained as

$$q_a = \frac{1}{\pi} \int_{\xi_w}^{\xi_c} \int_0^{2\pi} u_{a,Z} \hbar^2 \, d\phi \, d\xi, \tag{3.46}$$

$$q_c = u_{c,Z} R_i^2, \tag{3.47}$$

which must satisfy the zero net flux condition, i.e.

$$q_a + q_c = 0. \tag{3.48}$$

In this condition, the main unknown parameter of the flow is $f_a = (1/M)(\partial P_a / \partial Z)$ and $(\partial \tau_{c,ZZ} / \partial Z)$ (or $u_{c,Z}$), which can be computationally obtained using established nested iterations for multilayer viscoplastic flows (Taghavi *et al.* 2009; Taghavi 2018). The solution of the problem can be computed and it must satisfy the kinematic condition (Leal 2007), i.e.

$$\frac{\partial F}{\partial T} + \mathbf{u} \cdot \nabla F = 0, \tag{3.49}$$

which in combination with the continuity equation and some algebra translates to

$$\frac{\partial R_i^2}{\partial T} + \frac{\partial q_c}{\partial Z} = 0. \tag{3.50}$$

To find the interface motion versus time and space, the kinematic condition above (coupled to the other equations) is solved. To do so, an initially sharp interface is given at $Z = 0$,

typically following a sharp linear function $R_i^2(Z, T = 0) = -a(R_c^2/2)Z + R_c^2/2$ (with the coefficient $a = 10^3$). Let us recall that, here, $R_c = \hat{R}_c/\hat{R}$ is the inner radius of the injection pipe.

The discretization of the kinematic condition is implemented in conservative form, following a scheme that is first-order explicit in time and second-order in space, which for robust integration is coupled to a (shock-capturing) Van Leer flux limiter scheme (Yee, Warming & Harten 1985). To calculate $u_{c,Z}$, an integration scheme is employed.

3.4. Yielding length

Now, it is straightforward to obtain the critical yielding length, L_y , which is the length at which the viscoplastic core layer starts to yield at the inlet ($Z = 0$, where the stress is the highest). To do so, using (3.32) and the critical yield condition, i.e.

$$\frac{\sqrt{3}}{2}|\tau_{c,ZZ}| = B, \tag{3.51}$$

and knowing that $R_i = R_c$ and $u_{c,Z} = 1$ hold before yielding, we find

$$L_y = \frac{\sqrt{3}\delta B}{\left| -\frac{\partial P_a}{\partial Z} - \frac{1}{\pi R_c^2} \int_0^{2\pi} \hbar \tau_{a,\xi c Z} d\phi + \chi \right|}. \tag{3.52}$$

Accordingly, the yielding time is $T_y = L$. Also, f_a can be simply found by satisfying

$$\frac{1}{\pi} \int_{\xi_w}^{\xi_c} \int_0^{2\pi} u_{a,Z} \hbar^2 d\phi d\xi + R_c^2 = 0, \tag{3.53}$$

and, then, the shear stress $\tau_{a,\xi c Z}$ can be accordingly found using (3.45). Note that the sign of the denominator in (3.52) determines if the yielding occurs due to an extension or compression, i.e.

$$\left. \begin{aligned} \text{sgn} \left(-\frac{\partial P_a}{\partial Z} - \frac{1}{\pi R_c^2} \int_0^{2\pi} \hbar \tau_{a,\xi c Z} d\phi + \chi \right) > 0: \text{yielding due to extension} \Rightarrow \text{breakup}; \\ \text{sgn} \left(-\frac{\partial P_a}{\partial Z} - \frac{1}{\pi R_c^2} \int_0^{2\pi} \hbar \tau_{a,\xi c Z} d\phi + \chi \right) < 0: \text{yielding due to compression} \Rightarrow \text{buckling}. \end{aligned} \right\} \tag{3.54}$$

Also, the critical transition between the buckling (bulging) and breakup regimes occurs when the denominator in (3.52) becomes zero, i.e.

$$-\frac{\partial P_a}{\partial Z} - \frac{1}{\pi R_c^2} \int_0^{2\pi} \hbar \tau_{a,\xi c Z} d\phi + \chi = 0, \tag{3.55}$$

which corresponds to an infinitely long viscoplastic core layer, which is in a perfect balance of forces with no yielding.

The model presented in this section so far delivers the transition conditions from an unyielded to a yielded viscoplastic core fluid, for infinitely long core fluid (e.g. infinite falling height). The yielding can be due to the extensional or compressional stresses, eventually leading to the breakup or buckling (bulging) of the viscoplastic core, respectively. However, if the applied stresses on the core fluid perfectly

counterbalance one another, the core fluid does not buckle (bulge) nor break up, and it remains unyielded. On the other hand, considering a finite falling height (H), i.e. the case in our experiments, (3.52) delivers a yielding length (L_y) that can be compared with the falling height. Provided that the falling height is larger than the yielding length ($H > L_y/\delta$), the theory would suggest that the core fluid is yielded (due to extensional or compressional stresses depending on the parameters), leading to the breakup or buckling regimes. Conversely, if the falling height is smaller than the yielding length ($H \leq L_y/\delta$), the theory would suggest that the core fluid remains radially unyielded over the falling height (implying that the core fluid front theoretically can reach the pipe end without bucking/bulging or breakup), which would roughly translate to the coiling regime in the context of our experiments.

Considering its limit case, our theoretical result for the yielding length is consistent with those obtained from previous theoretical approaches for viscoplastic fluid flows injected in air (i.e. a dynamically inactive fluid). In this case, of course, the yielding would be always due to elongation not compression. If the annular fluid was ignored (as would be the case for the injection into air), the yielding length of (3.52) would become

$$\frac{L_y}{\delta} = \ell_y = \frac{\hat{\ell}_y}{\hat{R}} = \frac{\sqrt{3}B}{\chi} = \frac{\sqrt{3}\hat{\tau}_y}{(\hat{\rho}_c - \hat{\rho}_a)\hat{g}\hat{R}}, \tag{3.56}$$

which for air ($\hat{\rho}_a \ll \hat{\rho}_c$) becomes

$$\hat{\ell}_y \approx \frac{\sqrt{3}\hat{\tau}_y}{\hat{\rho}_c\hat{g}}. \tag{3.57}$$

The relation above is fully consistent with the yielding length obtained by Balmforth *et al.* (2010b) and Coussot & Gaulard (2005). In particular, the yielding length from Balmforth *et al.* (2010b) can be transferred to our scaling as

$$\hat{\ell}_y = \frac{\sqrt{3}\hat{\tau}_y}{\hat{\rho}_c\hat{g}} + \frac{\hat{\zeta}}{\hat{\rho}_c\hat{g}\hat{R}_c}, \tag{3.58}$$

in which $\hat{\zeta}$ denotes the surface tension. Note that the latter term that includes the surface tension effects is neglected in our miscible flow (which is also at the limit of large Pe).

3.5. Specific case of concentric injection flows

For concentric injection flows ($E = 0$), the bipolar coordinates (ξ, ϕ, Z) simplify to the cylindrical coordinates (r, θ, Z) . In this case, fully analytical expressions can be obtained for the quantities of interest, such as the pressure gradient and the interfacial shear stress, respectively:

$$f_a = \frac{1}{M} \frac{\partial P_a}{\partial Z} = \frac{-4u_{c,Z}}{\ln(R_i)R_i^2 - R_i^2 + \ln(R_i) + 1}, \tag{3.59}$$

$$\tau_{a,rZ} = \frac{u_{c,Z}M(1 - R_i^2)}{(\ln(R_i)R_i^2 - R_i^2 + \ln(R_i) + 1)R_i}, \tag{3.60}$$

where $\tau_{a,rZ} = \tau_{a,rZ}|_{r=R_c}$. The critical yielding length, L_y , can be also obtained straightforwardly:

$$L_y = \frac{\sqrt{3}\delta B}{\left| \frac{2M \left(2 + \left(\frac{1}{R_c^2} - 1 \right) \right)}{(\ln(R_c)R_c^2 - R_c^2 + \ln(R_c) + 1)} + \chi \right|}, \quad (3.61)$$

in which the denominator determines if the yielding occurs due to an extension or compression, i.e.

$$\left. \begin{aligned} \text{sgn} \left(\frac{2M \left(2 + \left(\frac{1}{R_c^2} - 1 \right) \right)}{(\ln(R_c)R_c^2 - R_c^2 + \ln(R_c) + 1)} + \chi \right) > 0: \text{yielding due to extension} \Rightarrow \text{breakup}; \\ \text{sgn} \left(\frac{2M \left(2 + \left(\frac{1}{R_c^2} - 1 \right) \right)}{(\ln(R_c)R_c^2 - R_c^2 + \ln(R_c) + 1)} + \chi \right) < 0: \text{yielding due to compression} \Rightarrow \text{buckling}. \end{aligned} \right\} \quad (3.62)$$

4. Model results and comparisons with experiments

4.1. Flow regimes

Let us begin with the transition boundaries between the breakup, coiling and buckling regimes. First of all, note that (3.52) gives a simple prediction to the onset of yielding of the viscoplastic core fluid, as a function of R_c , χ , B , M , $\delta \equiv 1/H$ and E (note that the onset of yielding is independent of the power-law index, n). Conservative critical boundaries between the regimes can be simply obtained by considering the critical yielding length to be equal to the falling height ($L_y/\delta = H$), which via rearranging (3.52) gives

$$\frac{MH}{B} = \frac{\sqrt{3}}{\left| -\frac{1}{M} \frac{\partial P_a}{\partial Z} - \frac{1}{\pi R_c^2 M} \int_0^{2\pi} \hat{h} \tau_{a,\xi c Z} d\phi + \frac{\chi}{M} \right|}, \quad (4.1)$$

where the first and second terms in the dominator, corresponding to the annular flow dynamics (i.e. the pressure gradient and shear stress terms), are directly calculated using the model. Thus, for given values of E and R_c , the two relevant dimensionless groups of the flow are

$$\frac{\chi}{M} = \frac{(\hat{\rho}_c - \hat{\rho}_a) \hat{g} \hat{R}^2}{\hat{\mu}_a \hat{V}_0}, \quad (4.2)$$

$$\frac{MH}{B} = \frac{\hat{\mu}_a \hat{V}_0 \hat{H}}{\hat{\tau}_y \hat{R}^2}. \quad (4.3)$$

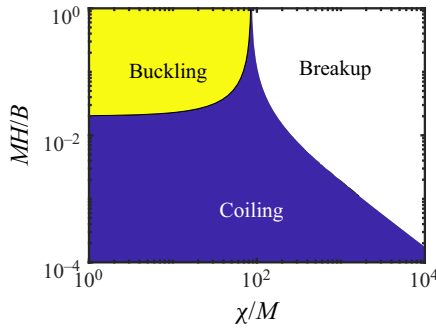


Figure 6. Regime classification in terms of the breakup, buckling (bulging) and coiling regimes in the plane of MH/B and χ/M , for $E = 0$ and $R_c = 0.5$, where different regimes are marked by different colours.

Note that, for concentric injection flows ($E = 0$), (4.1) reduces to a simplified analytical relation:

$$\frac{MH}{B} = \frac{\sqrt{3}}{\left| \frac{2 \left(2 + \left(\frac{1}{R_c^2} - 1 \right) \right)}{(\ln(R_c)R_c^2 - R_c^2 + \ln(R_c) + 1)} + \frac{\chi}{M} \right|}. \tag{4.4}$$

Before we proceed, let us clarify the discussion above on how to calculate the regime transition boundaries using the model. First of all, note that the model considers the yielding/non-yielding condition at the inlet of the core liquid since, prior to the yielding, the stresses are theoretically maximum at this location. From a theoretical perspective, this implies that, provided the core fluid does not yield at this location, it will not yield anywhere else in the pipe. Therefore, using the model, we can first calculate the transition boundaries between the core fluid flows which theoretically yield radially before reaching the pipe end and those which do not (using (4.1)). Once these transitions are identified, we can look at the sign of the denominator of (4.1) to theoretically categorize the yielding flows as breakup or buckling.

Figure 6 plots the theoretical critical boundaries via (4.1) in the plane of MH/B and χ/M (for fixed $E = 0$ and $R_c = 0.5$); the breakup, coiling and buckling regimes are marked. Each regime corresponds to a different balance among the governing forces that control the motion of the viscoplastic core. The breakup regime, where the viscoplastic core is yielded due to the extensional stress overcoming the yield stress, is found at large values of χ/M , corresponding to large buoyancy, low injection velocities and low viscosities of the annular fluid. The buckling regime, on the other hand, occurs at $\chi/M \lesssim O(10^2)$ and $MH/B \gtrsim O(10^{-2})$, representing small buoyancy, small yield stresses as well as large injection velocities and high viscosities of the annular fluid. In this regime, the yielding of the viscoplastic core towards buckling is due to the compressional stress dominating the yield stress. The area between the critical boundaries of the breakup and buckling regimes marks the coiling regime, where forces counterbalance one another in a way such that, theoretically, the viscoplastic core fluid neither breaks up nor buckles but, instead, shows a coiling behaviour. It is evident, from the regime map, that large yield stresses (large B) withstand extensional or compressional stresses, resulting in the coiling regime.

There exist alternative approaches to define the appropriate dimensionless groups, especially when dealing with viscoplastic fluids. In particular, if instead of $(\hat{\mu}_c \hat{V}_0)/\hat{R}$ we use $\hat{\tau}_y + (\hat{\mu}_c \hat{V}_0)/\hat{R}$ as the characteristic stress (Caliman, Soares & Thompson 2017), the

main dimensionless quantities change to

$$\left. \begin{aligned} B^* &= B \frac{(\hat{\mu}_c \hat{V}_0)/\hat{R}}{\hat{\tau}_y + (\hat{\mu}_c \hat{V}_0)/\hat{R}}, \\ M^* &= M \frac{(\hat{\mu}_c \hat{V}_0)/\hat{R}}{\hat{\tau}_y + (\hat{\mu}_c \hat{V}_0)/\hat{R}}, \\ \chi^* &= \chi \frac{(\hat{\mu}_c \hat{V}_0)/\hat{R}}{\hat{\tau}_y + (\hat{\mu}_c \hat{V}_0)/\hat{R}}. \end{aligned} \right\} \quad (4.5)$$

Using these new definitions, the main quantities employed to present the main results (e.g. the regime classification of figure 6) would not change, i.e.

$$\frac{\chi^*}{M^*} \equiv \frac{\chi}{M}, \quad (4.6)$$

$$\frac{M^* H}{B^*} \equiv \frac{MH}{B}. \quad (4.7)$$

Although the above-mentioned way of addressing the dimensionless analysis can be more aligned with the recent findings in yield stress materials, e.g. Kordalis *et al.* (2021) highlighting the advantages of using the plastic number (B^*) over the Bingham number (B), it does not change the outcomes of our work.

We have so far shown the existence of three main flow regimes, i.e. the breakup, coiling and buckling regimes, when a viscoplastic fluid is injected into a miscible medium (at the limit of large Pe), and we have accordingly delineated conservative transition boundaries between the flow regimes through the mathematical model, via the flow regime map in the plane of MH/B and χ/M (figure 6). Now, it is worth mentioning that, in terms of (4.1), there exist at least two obvious limit cases, i.e. $\chi/M = (\hat{\rho}_c - \hat{\rho}_a)\hat{g}\hat{R}^2/\hat{\mu}_a\hat{V}_0 \gg 1$ and $\chi/M = (\hat{\rho}_c - \hat{\rho}_a)\hat{g}\hat{R}^2/\hat{\mu}_a\hat{V}_0 \ll 1$, corresponding to the situations where the ambient fluid flow dynamics is either completely negligible or completely dominant, respectively. Regarding the former ($\chi/M \gg 1$), the viscoplastic fluid flow can only transition between the breakup and coiling regimes and the critical transition boundary can be simply obtained as

$$\frac{H}{B} \approx \frac{\sqrt{3}}{\chi}, \quad (4.8)$$

which relates, for example, the critical transition falling height (H) to the Bingham number (B) and the buoyancy number (χ). In this scenario, as B increases or χ decreases, the flow transitions from the breakup regime (where the viscoplastic core fluid breaks up) to the coiling regime (where the viscoplastic core fluid does not break up), while the ambient fluid flow dynamics does not play much of a role. From this perspective, therefore, the theory and the critical relation obtained can be directly used for much simpler flow configurations, e.g. the extrusion of a typical viscoplastic fluid into air (for which $\chi/M = (\hat{\rho}_c - \hat{\rho}_a)\hat{g}\hat{R}^2/\hat{\mu}_a\hat{V}_0 \gg 1$, since $\hat{\rho}_a$ and $\hat{\mu}_a$ are both very small, implying that air is practically a dynamically inactive fluid), albeit with ignoring the surface tension effects. This finding is consistent with the spirit of previous works (e.g. Coussot & Gaulard 2005; Balmforth *et al.* 2010a,b; Geffrault *et al.* 2021), which have mainly focused on the breakup of extruded viscoplastic fluids into air, although they have not typically considered/investigated a coiling regime due to unboundedness of their flow domains.

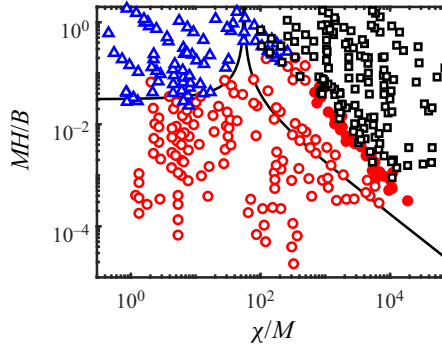


Figure 7. Comparison between the regime classifications based on the model (solid lines) and experiments (symbols, representing > 300 experiments) for $R_c = E = 1/3$, in the plane of MH/B and χ/M , for $R_c = E = 1/3$: the breakup regime (\square); the coiling regime (\circ); the buckling regime (Δ). The filled circle symbols mark the cases where the core fluid yields and thins but its front eventually reaches the pipe end before breakup, and starts coiling.

On the other hand, regarding the other limit in (4.1), i.e. $\chi/M \ll 1$, the viscoplastic fluid flow can only transition between the buckling and coiling regimes and the critical transition boundary can be simplified as

$$\frac{MH}{B} \approx c, \tag{4.9}$$

in which c is a constant, i.e. only dependent on E and R_c . Therefore, when the ambient fluid flow dynamics is dominant, the flow almost always belongs to the buckling regime, unless B is very large or H is very small.

4.2. Comparison with the experimental data

Figure 7 compares the three regimes based on the model and experiments. Despite the simplifying assumptions made in the model as well as complex experimental behaviours, the agreement between the model predictions and experiments is reasonable. However, some discrepancies are observed, e.g. the experimental coiling regime region is larger than that predicted by the model, a feature which may be justified. First, note that the critical condition of (4.1) is quite conservative and delivers only a prediction to the onset of yielding, which in the case of an extensional flow would not necessarily be equivalent to the breakup; in fact, when the core fluid yields near the inlet due to an extension, as the injection continues, the core fluid front can still evolve and reach the pipe end before the full breakup can occur. In this case, the coiling may occur for a core fluid that is partially yielded but not fully broken. Therefore, the experimental coiling (breakup) regime region is slightly larger (smaller) than that predicted by the model. On the other hand, yielding due to a compression almost certainly results in the buckling (bulging) regime because, in this case, the evolution of the core fluid front is significantly slowed down as the core fluid radially expands rapidly and cannot coil. This may justify why the model prediction to the transition between the buckling and coiling regimes may be more satisfactory.

As mentioned above, there are certain cases categorized within the coiling regime for which the core fluid is yielded but, due to the finiteness of the domain, its front reaches the pipe end before breaking up and starts coiling (see figure 4b). We have quantified and

marked such flows, using the filled symbols, in the regime map of [figure 7](#). Interestingly, such flows are all within the breakup regime zone predicted by the model, implying that the model can provide a good prediction to the yielding behaviour and these experiments would indeed exhibit a breakup for a longer falling height. We should also note that the coiling data points in [figure 7](#) include different sorts of observed coiling behaviours, i.e. regular, irregular and free coiling (as discussed in § 2).

Before we proceed, let us summarize some possible sources/reasons behind the experimental–modelling discrepancy observed in our work (see [figure 7](#)). (i) One of the possible reasons for the deviation of the experimental data from the model predictions (e.g. near the boundary of the coiling and breakup regimes) could be due to the yield stress values (obtained based on the HB model) used in our analysis. As shown earlier in § 2, the yield stresses obtained from the HB model fitting ([figure 2\(a\)](#) and [table 1](#)) are slightly different from those obtained using other measurement methods (e.g. compare [figures 2a, 2b, 2c](#) and [2d](#)). This difference highlights the fact that viscoplastic fluids are complex materials in terms of their yielding behaviour and that the yield stress measured using steady-state shear rheometry may not be the best choice across the board in different flow confirmations. (ii) Relevant to (i), a possible source of mismatch may be due to differences between extensional and viscometric yielding (which is the most widely used method to probe viscoplastic fluid rheology). For instance, Sica, de Souza Mendes & Thompson (2020) and Thompson & de Souza Mendes (2020) have considered extensional and compressional states of viscoplastic fluids extruded into air and they have quantified the corresponding yield stresses (namely static and dynamic yield stress values), which can be different from those delivered by steady-state shear rheometry. (iii) Another source of discrepancy between the model and experiments may be related to considering only normal components in the viscoplastic fluid flow and ignoring shear components in our asymptotic scaling analysis. Although in our work we may expect such an omission to have only negligible effects, there also are works in the literature (e.g. Moschopoulos *et al.* 2020; Geffrault *et al.* 2021) arguing that neglecting shear components of the strain rate tensor may lead to inaccuracies of slender filament approximations. (iv) Regarding the breakup regime, the discrepancy can also originate from the notion of yielding and rupturing in viscoplastic fluids (as also mentioned further above). Although the model may provide a reasonable understanding and prediction to the onset of yielding, the final rupturing of our viscoplastic fluid is hard to model and fully analyse, especially considering the multiphase nature of the flow. However, there are studies in the literature for simpler flow configurations (Hu *et al.* 2015; Tarcha *et al.* 2015; Thompson & de Souza Mendes 2020; Bahrani *et al.* 2021) which have investigated the rupturing of viscoplastic fluids but in different conditions; for instance, Tarcha *et al.* (2015) have analysed the yielding and rupturing of viscoplastic fluids using rheological tests, revealing how such fluids experience a destruction process and an eventual rupturing after the yield stress is overcome. (v) Finally, another discrepancy source is related to the nature of the model and experiment in our work. While the former is highly simplified, the latter is a complex flow, many features of which are ignored in the model for simplicity. For instance, the model does not obviously consider the coiling regime details (including regular, free and irregular coiling behaviours). In free coiling, in particular, the coiling starts before the core front touches the pipe end, i.e. a feature that is not included in the model and must be studied in future works.

A closer look at (3.52) reveals that, at the limit of a zero-injection velocity, the dimensional length of the viscoplastic core fluid at the yielding onset from the model

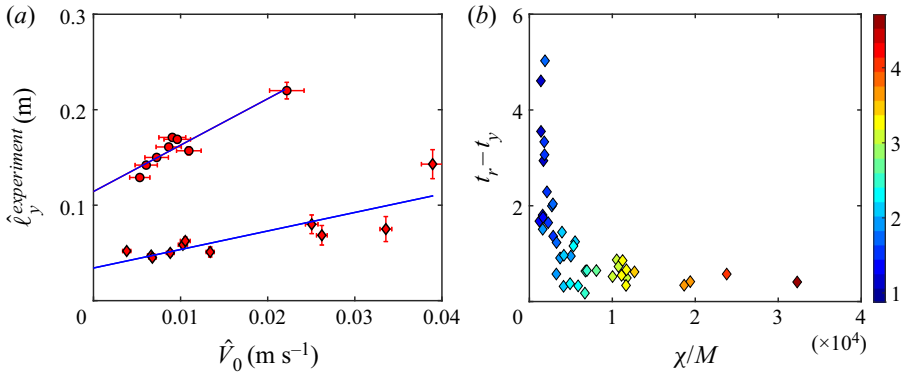


Figure 8. (a) Viscoplastic core length at the yielding onset $\hat{\ell}_y^{experiment}$ versus the injection velocity \hat{V}_0 for an injection flow in an eccentric pipe ($\hat{E} = 6.35$ mm). The symbols mark Sample III (circle) and Sample IV (diamond). The lines mark the least-squares fitting of the data points. Length $\hat{\ell}_y^{experiment}|_{\hat{V}_0 \rightarrow 0}$ is 0.115 and 0.039 m for Samples III and IV, respectively. (b) Dimensionless elapsed time between the yielding and rupturing $t_r - t_y$ versus χ/M for the breakup experiments for $E = 1/3$. The symbol colours represent the values of the Bingham number.

(ℓ_y) can be approximated as

$$\left. \frac{\hat{\ell}_y}{\hat{R}} \right|_{\hat{V}_0 \rightarrow 0} \approx \frac{\sqrt{3}B}{\chi} = \frac{\sqrt{3}\hat{\tau}_y}{(\hat{\rho}_c - \hat{\rho}_a)\hat{g}\hat{R}} \Rightarrow \hat{\ell}_y|_{\hat{V}_0 \rightarrow 0} \approx \frac{\sqrt{3}\hat{\tau}_y}{(\hat{\rho}_c - \hat{\rho}_a)\hat{g}}, \quad (4.10)$$

since the terms regarding the pressure gradient and the shear stress applied by the annular fluid flow vanish in (3.52) as $\hat{V}_0 \rightarrow 0$. Equation (4.10) can also provide a way to approximate the yield stress, provided that the yielding length is known at the limit of zero-injection rates. This approach has been previously demonstrated and used by Sica *et al.* (2020) and Thompson & de Souza Mendes (2020) in conceptually similar contexts. Figure 8(a) plots the length of the viscoplastic core at the yielding onset from the experiments ($\hat{\ell}_y^{experiment}$) for small injection velocities. In this figure, the symbols mark Sample III (circles) and Sample IV (diamonds). As can be seen, $\hat{\ell}_y^{experiment}$ for Sample III is larger than that for Sample IV. Following Sica *et al.* (2020) and Thompson & de Souza Mendes (2020), it is possible to use a linear least-squares fit as a crude way to estimate the yielding length at the limit of the zero-injection velocity, namely where the fitted line crosses the vertical axis, i.e. $\hat{\ell}_y^{experiment}|_{\hat{V}_0 \rightarrow 0}$. Accordingly, using (4.10), the associated yield stresses for Samples III and IV can be approximated as 6.47 and 4.31 Pa, respectively, which in comparison with the rheometry results (table 1) show a difference of less than 7%.

For the sake of completeness of the result presentation, let us show the dimensionless elapsed time between the yielding onset ($t_y = \hat{t}_y/(\hat{R}/\hat{V}_0)$) and the eventual of breakup or rupturing ($t_r = \hat{t}_r/(\hat{R}/\hat{V}_0)$) of the core viscoplastic fluid, as shown in figure 8(b) for our experimental results. The yielding and rupturing times are extracted from the experimental data using an image processing technique. This figure shows $t_r - t_y$ versus χ/M , while the values of the Bingham number are superimposed by the symbol colours. The results show that, by increasing χ/M and B , the elapsed time decreases, i.e. the core fluid ruptures faster. The results for the elapsed time between yielding and rupturing, such as those

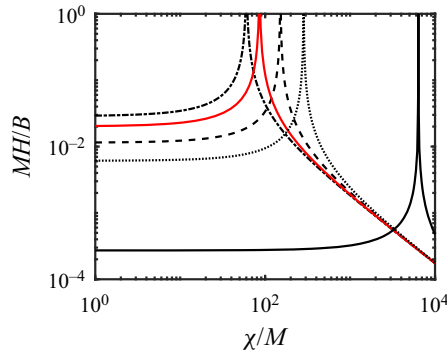


Figure 9. Critical regime transition boundaries in the plane of MH/B and χ/M , for $E = 0$ and $R_c = 0.1$ (dashed line), 0.3 (dash-dotted line), 0.5 (red solid line), 0.7 (dotted line) and 0.9 (black solid line).

presented in figure 8(b), could be perhaps further analysed in future works to distinguish between two critical stresses, i.e. associated with yielding and rupturing.

4.3. Effect of R_c

It is insightful to study the effects of the variation of R_c on the regime boundaries, as shown in figure 9. As seen, varying R_c can significantly change the regime boundary positions, albeit in a non-monotonic way; by increasing R_c up to 0.3, the critical boundaries are shifted to the left but, for higher values of R_c , they are moved to the right. In the latter case, the buckling regime region becomes significantly wider.

The model predicts a non-monotonic effect of R_c on the critical regime boundaries, especially in terms of the transition between the buckling and breakup regimes. In an attempt to explain this non-monotonic behaviour, let us consider a long core fluid, for which R_c increases from small values, while the other parameters are fixed. On the one hand, note that the buoyancy force is the only force that pulls the core fluid downward, while the other forces (including the yield stress force and the shear stress force at the interface) resist against this force and, therefore, against the breakup. On the other hand, the buoyancy force per unit volume is constant (proportional to χ), while the interfacial shear force per unit volume is proportional to $(1/R_c)(\tau_{a,rZ}/M)$. Therefore, initially at small R_c , the interfacial shear force per unit volume decreases with increasing R_c . However, as R_c keeps increasing and the annular flow cross-section area decreases, the shear stress applied at the interface increases due to the flux constraint. This results in the interfacial shear force per unit volume eventually increasing at larger R_c , implying that a larger χ would be needed to overcome this force and lead to the transition from the buckling regime to the breakup regime.

To better illustrate the discussion above, figure 10 presents the variation of three parameters versus the core fluid radius. To simplify the analysis, the condition before yielding ($R_i = R_c$ and $u_{c,Z} = 1$) for a concentric flow ($E = 0$) is considered. The solid black line marks the non-monotonic variation of $|(1/R_c)(\tau_{a,rZ}/M)|$ versus R_c , i.e. initially decreasing and then increasing as R_c grows. The variation of $(1/M)(\partial P_a/\partial Z)$ versus R_c (the red dashed line) shows that, as may be expected, the pressure gradient increases monotonically as R_c increases. Also, at large R_c , the value of $(1/M)(\partial P_a/\partial Z)$ progressively increases and dominates that of $|(1/R_c)(\tau_{a,rZ}/M)|$. Finally, the variation of $(\chi/M)_{critical}$ versus R_c is also shown. For an infinitely long viscoplastic core layer,

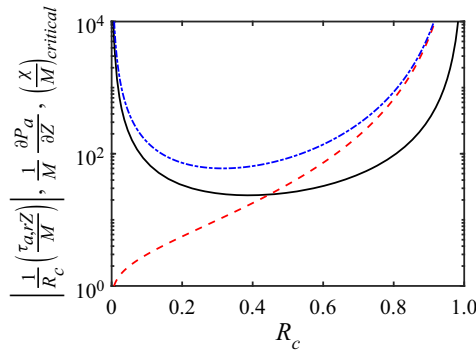


Figure 10. Variation of $|(1/R_c)(\tau_{a,rZ}/M)|$ (solid black line), $(1/M)(\partial P_a/\partial Z)$ (red dashed line) and $(\chi/M)_{critical}$ (blue dash-dotted line) versus R_c for $E = 0$.

$(\chi/M)_{critical}$ delineates the critical transition between the buckling and breakup regimes (i.e. simply found by setting the denominator of (3.62) equal to zero). A final note inferred from figure 10 is that, as R_c approaches the value of zero or one, $|(1/R_c)(\tau_{a,rZ}/M)|$ and $(\chi/M)_{critical}$ approach large values, implying that the model may not be valid as R_c approaches its extreme values.

Figure 11(a) shows the regime classification in the plane of R_c and χ/M for an infinitely long pipe. The flow configuration is concentric (i.e. $E = 0$). The black solid line delineates the transition between the breakup and buckling regimes; there is, of course, no coiling regime and the line itself represents a core fluid layer that never breaks up or buckles in an infinitely long pipe. Figure 11(b) shows the regime transition boundaries for different values of MH/B . For $MH/B = \infty$, there is no coiling regime but, as MH/B decreases, the coiling regime region appears and expands in the area sandwiched between the buckling and breakup regimes (corresponding to the dashed and dash-dotted lines). Moreover, for the ranges observed, the transition boundary has a minimum value of χ/M for a core with $R_c \approx 0.3$. Figure 11(c) depicts the regime classification for a typical finite value of $MH/B = 0.01$. As seen, for a given value of R_c , on increasing χ/M , the flow transitions from the buckling to coiling and eventually to the breakup regime. Also, interestingly, for $0.10 \lesssim R_c \lesssim 0.64$ and all the values of $\chi/M \geq 1$, the viscoplastic core fluid does not buckle.

4.4. Effect of E

Figure 12(a–d) shows the regime classification in the plane of R_c and χ/M , for an infinitely long pipe and different eccentricities. The black solid line delineates the transition between the breakup regime (on the right-hand side) and the buckling regime (on the left-hand side). In an infinitely long pipe, there is no coiling regime and each line for different E represents a core fluid layer that never breaks up or buckles. It should be noted that, with increasing eccentricity, the variation of R_c becomes limited. It can be seen that, with increasing E , the buckling regime region is expanded. Figures 12(e) and 12(f) show observations similar to those in figures 11(b) and 11(c), respectively, but for an eccentric flow ($E = 0.4$).

Figure 13 illustrates a comparison between the results obtained for the two different values of E . The lines and data points represent the modelling and experimental results, respectively. For $R_c = 1/3$, for the value of which the experimental results are also superimposed, the coiling regime is seen for smaller values of χ/M when $E = 0$.

Breakup, coiling and buckling in viscoplastic injections

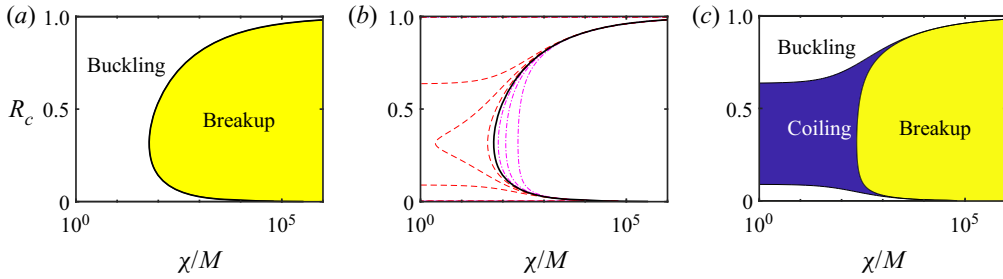


Figure 11. Regime classification for an infinitely long pipe for $E = 0$. (a) The regime classification of breakup and buckling for an infinitely long pipe. The thick solid line marks the critical transition. (b) Contour values of MH/B for $E = 0$. The thick solid line marks $MH/B = \infty$. The dash-dotted lines correspond to yielding (breakup) due to extension, where $MH/B = 0.1, 0.03$ and 0.01 , from left to right. The dashed lines correspond to yielding (buckling) due to compression, where $MH/B = 0.1, 0.03$ and 0.01 , from right to left. (c) Regime classification of the breakup, coiling and buckling regimes, in a pipe with the typical length of $H = (1/100)(B/M)$.

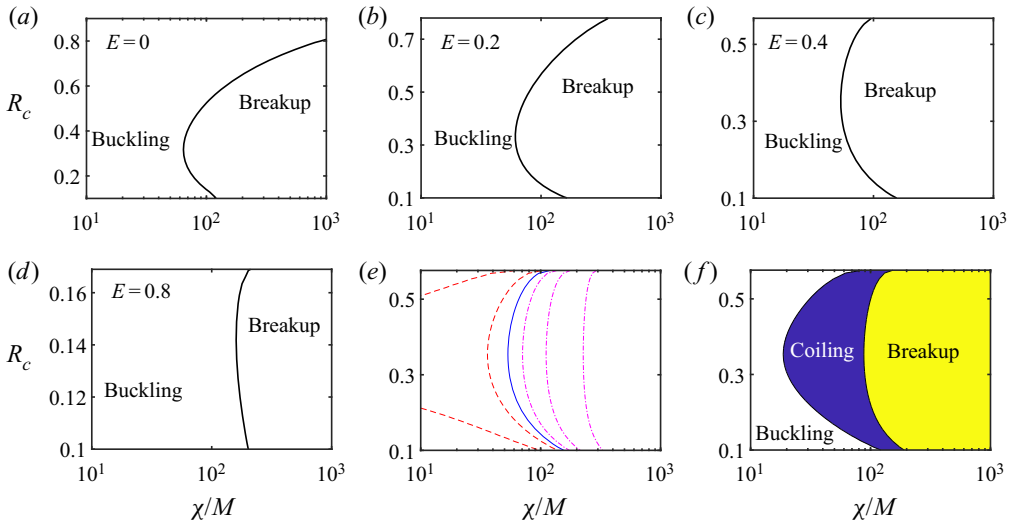


Figure 12. Regime classification for an infinitely long pipe for various eccentricities: (a) $E = 0$, (b) $E = 0.2$, (c) $E = 0.4$ and (d) $E = 0.8$. (e) Contour values of MH/B for $E = 0.4$. The thin solid line marks $MH/B = \infty$. The dash-dotted lines correspond to yielding (breakup) due to extension, where $MH/B = 0.1, 0.03$ and 0.01 , from left to right. The dashed lines correspond to yielding (buckling) due to compression, where $MH/B = 0.1, 0.03$ and 0.01 , from right to left. (f) Regime classification of the breakup, coiling and buckling regimes in a pipe with typical length of $H = (1/20)(B/M)$.

In addition, the comparison between the experimental and modelling results shows reasonable agreement.

4.5. Interface evolution and velocity field

Figure 14 depicts typical examples of the evaluation of a core fluid interface, at a given time T , in the absence and presence of the annular flow dynamics, for a concentric flow configuration. As seen, when the core fluids are yielded, the stress contours exceed B everywhere, except for the core fluid's lowest part. Figures 14(a) and 14(c) show that,

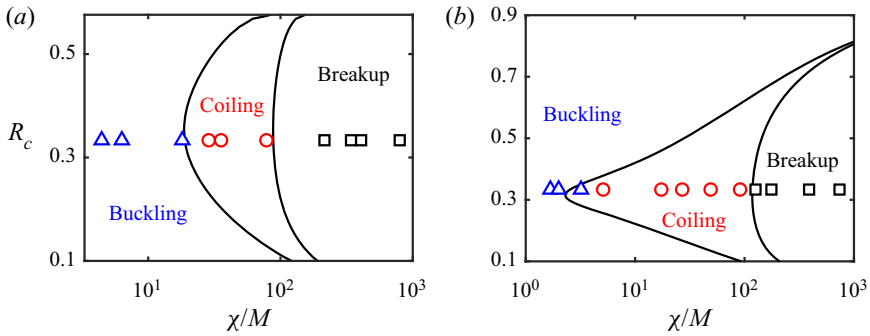


Figure 13. Regime classification based on the model (lines) and experiments (symbols) for (a) $E = 1/3$, $H = (1/20)(B/M)$ and (b) $E = 0$, $H = (3/100)(B/M)$. The bounded regions via lines show the breakup, coiling and buckling regimes from right to left, respectively. Different symbol shapes represent the breakup regime (\square), the coiling regime (\circ) and the buckling regime (Δ) in the experiments.

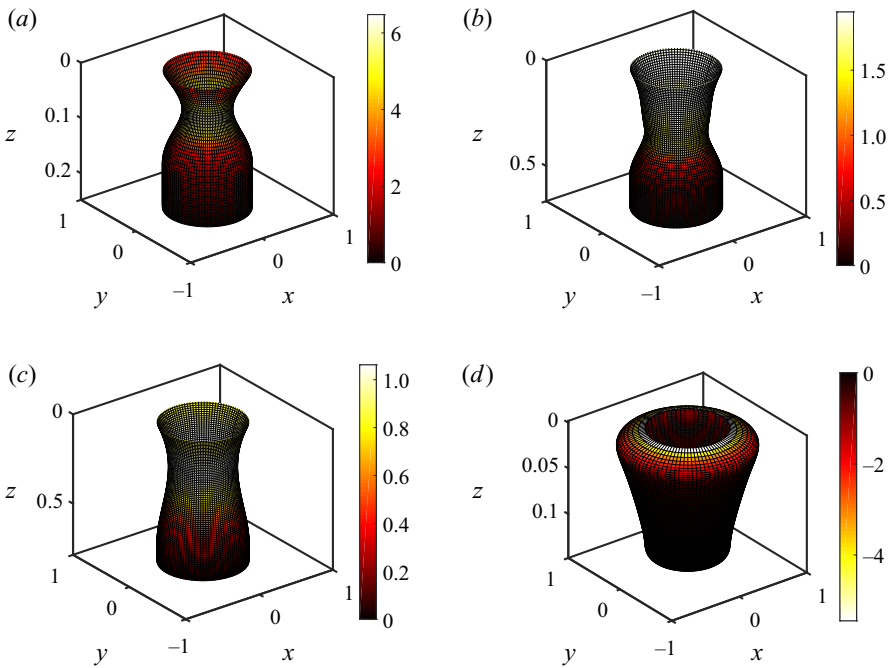


Figure 14. Interface evolution for $\delta = 0.05$, $n = 0.5$, $R_c = 0.5$ and $E = 0$ (a,c) without and (b,d) with considering the annular flow dynamics: (a,b) $B = \chi = 1$ and $M = 0.005$; (c,d) $B = \chi = 0.1$ and $M = 0.02$; (a) $T = 0.19$, (b) $T = 0.5$, (c) $T = 0.6$ and (d) $T = 0.24$. The superimposed colours and the colour bars represent the values of $\tau_{c,ZZ}$.

without the annular flow, the extensional stress (positive $\tau_{c,ZZ}$) dominates the yield stress in the thinning region, as the core progresses towards the breakup. When the annular flow dynamics is considered, and depending on the values of χ , B and M (for fixed δ , E , R_c and n), figures 14(b) and 14(d) reveal that the flow can transition between the breakup and buckling regimes. For instance, for small M , the extensional stress (positive $\tau_{c,ZZ}$) is dominant, while for large M the compressional stress (negative $\tau_{c,ZZ}$) becomes dominant.

Breakup, coiling and buckling in viscoplastic injections

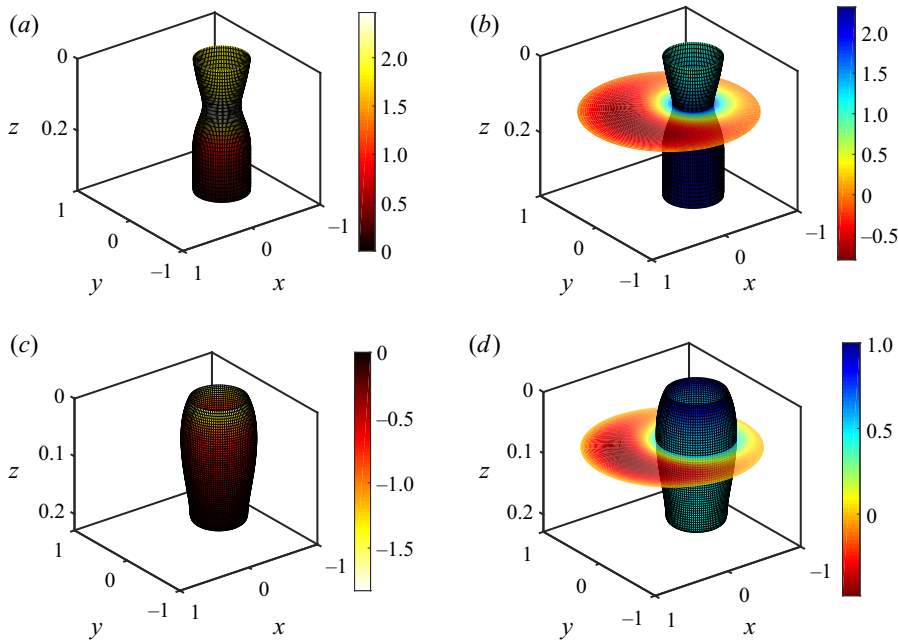


Figure 15. Model results of an eccentric injection, for $\delta = 0.05$, $n = 0.5$, $R_c = E = 1/3$ and $T = 0.3$: (a,b) $B = \chi = 1$ and $M = 0.005$; (c,d) $B = \chi = 0.1$ and $M = 0.02$. (a,c) Interface shape, along with $\tau_{c,ZZ}$ superimposed as colours. (b,d) Interface shape, along with axial velocity (u_z) superimposed as colours. The core fluid velocity is given throughout the viscoplastic layer length while the annular velocity is given at $Z \approx L/3$.

Figure 15 presents the interface shape, along with the dominant stress contours (figure 15a,c) and the axial velocity contours (figure 15b,d), for compressional and extensional flows of an eccentric viscoplastic core flow ($E = 1/3$), at a given time T . Figures 15(a,b) and 15(c,d) correspond to the breakup and buckling regimes, respectively. In figures 15(a,c) and 15(b,d), the values of $\tau_{c,ZZ}$ and $u_{c,Z}$ are superimposed on the interface shape, respectively. Additionally, in figure 15(b,d), the annular flow velocity field near the necking/buckling region is also superimposed. As seen, increasing the viscosity of the annular fluid causes the extensional stress (positive $\tau_{c,ZZ}$) to become a compressional stress (negative $\tau_{c,ZZ}$); this leads to the transition of the flow dynamics from the breakup to the buckling regime. In both regimes, however, the unyielded region ($|\tau_{c,ZZ}| \leq B$) is located near the core end, with lower velocity for the buckled core. Figure 15 also shows that, in the buckling regime, the core fluid layer grows much slower (note that all the results are at $T = 0.3$). Also, for the breakup flow, the core velocity has the lowest value at the inlet, while for the buckling flow the core fluid velocity is highest near the inlet. In addition, the local velocity of the annular fluid is larger in the wide side of the eccentric core than that in the narrow side. As the eccentricity promotes the flow along the wide side, it affects on the dynamics of the injected viscoplastic core fluid, through changing the interfacial stresses due to the upward motion of the annular fluid. Finally, our results show that the predictions of the interface evolution using the model are in qualitative agreement with the early-time experimental interface shapes in the breakup and buckling regimes; see figure 1(b₁–b₃).

In order to gain more insight into the flow, here, let us further analyse the core fluid behaviour without and with considering the annular fluid flow dynamics, as shown in

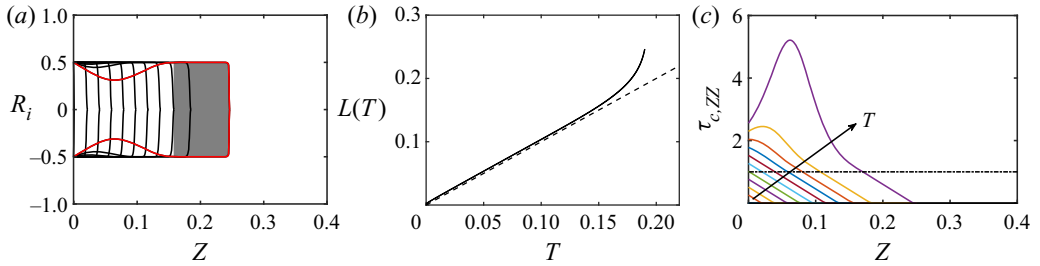


Figure 16. Model results for the dynamics of a breakup flow, for a case without considering the annular flow dynamics. The flow parameters are $\delta = 0.05$, $n = 0.5$, $B = \chi = 1$, $R_c = 0.5$ and $T_{end} = 0.19$. (a) Interface radius R_i versus Z and T . The results are shown for $T = 0, T_{end}/10, \dots, 9T_{end}/10, T_{end}$. The last profile is marked by the red line, for which the shaded area marks the unyielded region. (b) The viscoplastic fluid layer length $L(T)$ versus time T . The dashed line is for comparison purposes and marks $L(T) = T$. (c) Plot of $\tau_{c,ZZ}$ versus Z and T . The solid arrow shows the increase in time T . The results are shown for $T = 0, T_{end}/10, \dots, 9T_{end}/10, T_{end}$. The horizontal dash-dotted line marks $\tau_{c,ZZ} = B$.

figures 16 and 17, respectively. The former (i.e. when the annular fluid flow dynamics is ignored) would resemble the simpler case of the injection of a viscoplastic fluid into a dynamically inactive fluid, such as air (Coussot & Gaulard 2005; Balmforth *et al.* 2010*a,b*; Geffraut *et al.* 2021), albeit with ignoring surface tension effects. Figure 16(a) shows the variation of the interface radius along the length of the core versus the time. At long times, the core fluid yields after advancing some distance with respect to the injection inlet (when, loosely speaking, a sufficient weight of the core fluid is hung below the injection inlet). Meanwhile, as time progresses, the core fluid becomes thinner at the yielding point. The core is yielded, except for a small region towards its front. Figure 16(b) shows the growth of the core fluid length (L) versus time (T), which occurs due to the continuous injection of the viscoplastic fluid. Initially, before yielding, the layer length varies linearly with time. After yielding, however, $L(T)$ deviates from the linear line of $L(T) = T$, and grows more rapidly as expected. A sequence of profiles illustrating $\tau_{c,ZZ}$ along the core length are shown in figure 16(c), for the corresponding times in figures 16(a) and 16(b). The horizontal dash-dotted line in figure 16(c) represents the value of B . At early times, the magnitude of $\tau_{c,ZZ}$ along the core length shows a gradual increase with time. Before yielding ($\tau_{c,ZZ} \leq B$), the maximum stress is at $Z = 0$, which represents the injection inlet. Nevertheless, after yielding ($\tau_{c,ZZ} > B$), the point where the stress is maximum moves downward as time increases. Finally, considering the observations made in figure 16, very similar behaviours are observed when buoyancy is large while the annular flow dynamics is considered.

Figure 17(a) shows the variation of the interface radius along the core length for different times in the presence of the annular flow. It can be observed that the inclusion of the annular flow creates sufficient viscous stresses for yielding and buckling of the core fluid, as a yielded region appears adjacent to the point of injection, where the compressive stress overcomes the yield stress. While the core fluid buckles radially, we can observe that the core fluid front section remains unyielded. As seen in figure 17(b), at early times, the growth rate of the viscoplastic layer length is constant, until the time at which the yielding and buckling of the core occur. After yielding, however, $L(T)$ deviates from the linear line of $L(T) = T$, and grows more slowly as expected. The variation of the stresses along the core in each time step is depicted in figure 17(c), showing a gradual increase in the stress magnitude with time. Since B is small, $\tau_{c,ZZ}$ quickly overcomes B and core fluid yields radially. Comparing figures 17(c) and 16(c) shows that the signs of $\tau_{c,ZZ}$ are opposite in

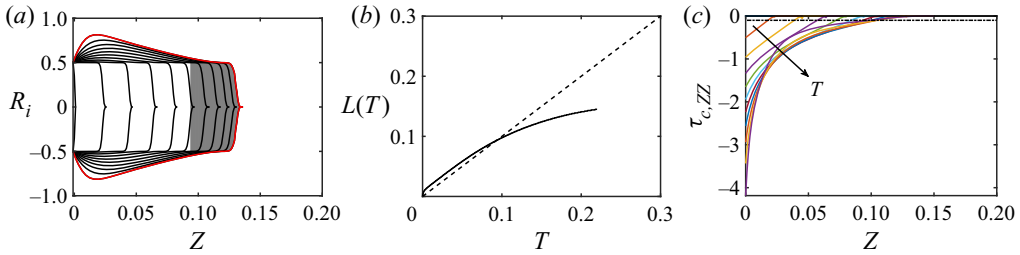


Figure 17. Model results for the dynamics of a buckling flow, while considering the annular flow dynamics. The flow parameters are $\delta = 0.05$, $n = 0.5$, $B = 0.1$, $\chi = 0$, $R_c = 0.5$, $M = 0.02$, $E = 0$ and $T_{end} = 0.22$. (a) Interface radius R_i versus Z and T . The results are shown for $T = 0, T_{end}/10, \dots, 9T_{end}/10, T_{end}$. The last profile is marked by the red line, for which the shaded area marks the unyielded region. (b) The viscoplastic fluid layer length $L(T)$ versus time T . The dashed line is for comparison and shows $L(T) = T$. (c) Plot of $\tau_{c,ZZ}$ versus Z and T . The solid arrow shows the increase in time T . The results are shown for $T = 0, T_{end}/10, \dots, 9T_{end}/10, T_{end}$. The horizontal dash-dotted line marks $\tau_{c,ZZ} = -B$.

these figures, which is trivial. However, comparing figures 16(c) and 17(c) reveals that the maximum value of the stress remains always close to $Z = 0$, even after yielding (at least for the case considered).

The results presented in this section on the interface dynamics, obtained using the model, reveal that our theoretical predictions of the interface shape and its evolution are in agreement, albeit rather very qualitative, with the shape of the thinning region in the extensional flow or the buckling region in the compressional flow, e.g. as observed in our experiments; see e.g. figure 3.

5. Summary and concluding remarks

Our experiments reveal the existence of the breakup, coiling and buckling (bulging) regimes in the vertical injection of a heavy viscoplastic fluid into a closed-end pipe filled with a Newtonian fluid. Accordingly, we develop and validate a lubrication approximation model to predict the flow regime boundaries. The model parameters include $\delta \equiv 1/H$, n , R_c , E , B , χ and M (see table 3 for the definitions). Based on analysing the yielding behaviour of the viscoplastic fluid, the model delivers a conservative prediction to the regime classification in the plane of MH/B and χ/M . The breakup regime is observed at large χ/M , where the viscoplastic fluid undergoes an extension, yields and eventually breaks up due to large buoyancy. The buckling regime is seen at small χ/M where the viscoplastic fluid is yielded, and radially expands, due to compressional stresses caused by the annular flow dynamics. When the viscoplastic fluid neither breaks up nor radially buckles (bulges), it can lead to the coiling regime where the viscoplastic core fluid shows coiling behaviours.

It can be insightful to strengthen the positioning of our work/results with respect to previous works, e.g. those concerning the injection of viscoplastic fluids into air (Coussot & Gaulard 2005; Balmforth *et al.* 2010a,b; Rahmani *et al.* 2011; Balmforth & Hewitt 2013; Geffraut *et al.* 2021), discussed in the introduction. In general, the following aspects can be highlighted. First, note that our flow is a buoyant multiphase flow in nature, i.e. the dynamics of our two fluid flows are interconnected and strongly affect each other. This is because, in contrast with previous works considering air as the surrounding fluid, the ambient fluid considered in our work remains an active *in situ* fluid, whose flow dynamics along with its properties can significantly affect the viscoplastic fluid flow.

Second, our work brings the effects of transverse and longitudinal geometry confinements (motivated by industrial application, e.g. in P&A processes) into the analysis. This leads to an exchange flow configuration in a given cross-section of the flow; as the viscoplastic filament moves downward, the Newtonian ambient fluid flow moves mostly upward. This, in return, produces a pressure gradient and a stress at the interface, which affect the interfacial flow dynamics, e.g. via modifying the viscoplastic fluid yielding length condition. Considering this argument, let us briefly explain how the flow regimes, studied and understood in the context of viscoplastic fluid injections into air, can be affected when air (as the ambient fluid) is replaced by a dynamically active liquid in our confined flow configuration. (i) Regarding the breakup regime, the general yielding mechanism is similar to that in air, in the sense that buoyancy (in other words gravity) eventually dominates the yield stress and leads to yielding, extension and eventually breakup (Coussot & Gaulard 2005; Balmforth *et al.* 2010a,b; Geffraut *et al.* 2021). However, the viscoplastic filament flow, the interface motion, the yielding length and the breakup are also expectedly affected by the ambient fluid flow dynamics (e.g. via the dimensionless numbers such as M and χ). The flow can be also particularly affected in terms of the evolution of the yielded region and the progression towards pinch-off, the detailed analysis of which we leave to future works. (ii) While our coiling regime generally resembles that observed in some previous works on viscoplastic injections into air (Rahmani *et al.* 2011), note that we have not much analysed this regime and its dynamics, except for proposing a regime zone (in terms of the dimensionless numbers) when it may occur, based on using the model prediction to the yielding length. However, our work shows that the ambient fluid flow dynamics can be used to significantly promote/delay the occurrence of the coiling regime, i.e. a finding which can be perhaps extended in future studies to control the flow behaviours in this regime. (iii) Finally, the buckling (bulging) regime found in our work is not much studied in the literature and it does not have a direct counterpart in the case of viscoplastic fluid injections into air. As mentioned in the introduction, the ‘buckling’ observed in injections into air typically occurs in upward injections when the viscoplastic fluid yields and bends sideways, after a critical length, loosely speaking due to its weight overcoming the yield stress (Balmforth & Hewitt 2013). Nevertheless, in our case, the yield stress is overcome and the viscoplastic fluid radially expands and buckles (bulges), obviously not because of its weight but because of the pressure gradient and stress applied at the interface caused by the ambient fluid flow dynamics. This flow regime should be, of course, further studied in future to reveal its intricacies and complex dynamics, especially at longer times.

The combination of the model and experiments developed in this work could be extended in future, perhaps as a rheometrical approach, to measure extensional (elongation and compression) rheological properties of viscoplastic fluids. For instance, the breakup regime, which is dominated by normal stresses associated with extension, can reveal viscoplastic fluids’ elongation properties, based on analysing the deformation and breakup of viscoplastic filaments due to buoyancy. This would extend, for example, the recent interesting work of Geffraut *et al.* (2021) who have developed, for dynamically inactive ambient fluids, an extensional gravity–rheometry approach, via calculating the normal stress from the acceleration and weight of viscoplastic materials. In addition, our experiments have some conceptual similarities to those recently conducted by Sica *et al.* (2020) (for dynamically inactive ambient fluids), who analysed the yielding of several materials in elongation and compression loading conditions, while proposing new criteria for yielding. In the former condition, gravity is the main source of the induced stress that eventually overcomes the yield stress. Similar to and extending these aforementioned studies, our approach could be potentially used to quantify an extensional yield stress.

Although the focus of the current work is on relatively large-scale filaments, in miscible multiphase flows (at the limit of large Pe), where surface tension effects are not relevant, other future works may perform similar experiments/modelling with immiscible flows at smaller sizes where these effects could become important. In general, the current model and experiments can be extended to consider the capillary effects. In this scenario, one would expect the interface curvature and the accompanying capillary pressure to affect the flow dynamics. For instance, a capillary number (e.g. defined as the ratio of the extrusion time scale to viscous–capillary reaction time scale) would appear as an additional parameter, governing the yielding length, the regime transition boundaries and the interface evolution dynamics. In particular, one may expect that, by including the capillary pressure, the filament can resist further against yielding and can advance a larger extrusion length before yielding, resulting in delaying the transition to the breakup and buckling regimes.

Note that the experimental flow of our consideration (i.e. a buoyant miscible injection of a viscoplastic fluid into a pipe filled with a Newtonian fluid) is a highly complex flow phenomenon (in other words, a complex flow of a complex fluid). Therefore, we certainly do not (and must not) claim that we have analysed, quantified and understood all the relevant flow features and complex flow aspects in this single study. Instead, our work should be principally viewed as a straightforward model to roughly predict some of the leading-order phenomena, e.g. in terms of the transition boundaries between some of the main flow regimes, observed in our experiments. For instance, various flow behaviours classified for simplicity under the umbrella of the coiling regime (including regular, free and irregular coiling) must be experimentally studied in detail in future. Therefore, future research directions should be directed towards understanding various complex flow features, the details of each identified regime, the flow subregimes, the longer-time flow dynamics, as well as developing a more sophisticated model with a rigorous inclusion of inertial terms. Studies along these lines are ongoing in our research group.

Acknowledgements. We thank R. Bardestani at Université Laval for helping us in designing the schematic of the experimental apparatus. We also thank J. Noël and J.N. Ouellet (department technicians) for the construction of the experimental apparatus and useful technical discussions. Finally, we thank anonymous reviewers for their invaluable comments and suggestions, which resulted in improving the manuscript.

Funding. We acknowledge the financial support provided by PTAC-AUPRF via grant no. PTAC-17-WARI-02, and the Natural Sciences and Engineering Research Council (NSERC) via CRDPJ 516022-17 (‘Plug and Abandon Strategies for Canada’s Oil and Gas Wells’). We also acknowledge the support of the Canada Research Chair (CRC) on Modeling Complex Flows, and the infrastructure support provided by the Canada Foundation for Innovation (CFI).

Declaration of interests. The authors report no conflict of interest.

Author ORCIDs.

 S.M. Taghavi <https://orcid.org/0000-0003-2263-0460>.

Appendix A. Solution of Newtonian annular flow velocity and shear stress

In this appendix, we derive the solutions to the velocity and shear stress fields of the annular fluid flow, based on appropriate boundary conditions. Following from (3.43), the no-slip boundary condition at the pipe wall gives

$$\begin{aligned}
 u_{a,Z}(T, \xi_w, \phi, Z) &= u_{ah,Z}(T, \xi_w, \phi, Z) + u_{ap,Z}(T, \xi_w, \phi, Z) = 0 \\
 \Rightarrow u_{ah,Z}(T, \xi_w, \phi, Z) &= -u_{ap,Z}(T, \xi_w, \phi, Z) = -\frac{f_a \sinh^2 \xi_w \cosh \xi_w}{2(\cosh \xi_w - \cos \phi)}. \quad (\text{A1})
 \end{aligned}$$

Accordingly, we find

$$[\alpha_{a0} \cosh(m\xi_w) + \beta_{a0} \sinh(m\xi_w)]_{m=0} + \sum_{m=1}^{\infty} [\alpha_{am} \cosh(m\xi_w) + \beta_{am} \sinh(m\xi_w)] \cos m\phi = -\frac{f_a \sinh^2 \xi_w \cosh \xi_w}{2 \cosh \xi_w - \cos \phi}. \tag{A2}$$

We multiply both sides of the equation above by $\cos(m\phi)$, integrate over $0 \leq \phi \leq 2\pi$ and after some algebra arrive at

$$\left. \begin{aligned} \alpha_{a0} &= -\beta_{a0} \tanh(m\xi_w) - \frac{f_a \sinh \xi_w \cosh \xi_w}{2}, \quad m = 0, \\ \alpha_{am} &= -\beta_{am} \tanh(m\xi_w) - \frac{f_a \sinh \xi_w \cosh \xi_w e^{-m\xi_w}}{\cosh(m\xi_w)}, \quad m \geq 1. \end{aligned} \right\} \tag{A3}$$

The velocity at the interface should be continuous, i.e.

$$u_{a,Z}(T, \xi_c, \phi, Z) = u_{c,Z}(T, Z), \tag{A4}$$

giving

$$\begin{aligned} u_{a,Z}(T, \xi_c, \phi, Z) &= u_{ah,Z}(T, \xi_c, \phi, Z) + u_{ap,Z}(T, \xi_c, \phi, Z) = u_{c,Z}(T, Z) \Rightarrow \\ u_{ah,Z}(T, \xi_c, \phi, Z) &= -u_{ap,Z}(T, \xi_c, \phi, Z) + u_{c,Z}(T, Z) \\ &= -\frac{f_a \sinh^2 \xi_w \cosh \xi_c}{2(\cosh \xi_c - \cos \phi)} + u_{c,Z}(T, Z). \end{aligned} \tag{A5}$$

Accordingly, we find

$$[\alpha_{a0} \cosh(m\xi_c) + \beta_{a0} \sinh(m\xi_c)]_{m=0} + \sum_{m=1}^{\infty} [\alpha_{am} \cosh(m\xi_c) + \beta_{am} \sinh(m\xi_c)] \cos m\phi = -\frac{f_a \sinh^2 \xi_w \cosh \xi_c}{2(\cosh \xi_c - \cos \phi)} + u_{c,Z}. \tag{A6}$$

We multiply both sides of the equation above by $\cos(m\phi)$, integrate over $0 \leq \phi \leq 2\pi$ and after some algebra arrive at (note that the integral of $u_{c,Z} \cos(m\phi)$ is zero except for $m = 0$)

$$\left. \begin{aligned} \alpha_{a0} &= -\beta_{a0} \tanh(m\xi_c) - \frac{f_a \sinh^2 \xi_w \cosh \xi_c}{2 \sinh \xi_c} + u_{c,Z}, \quad m = 0, \\ \alpha_{am} &= -\beta_{am} \tanh(m\xi_c) - \frac{f_a \sinh^2 \xi_w \cosh \xi_c e^{-m\xi_c}}{\sinh \xi_c \cosh(m\xi_c)}, \quad m \geq 1. \end{aligned} \right\} \tag{A7}$$

Using the relations obtained above, we can find explicit relations for the coefficients as follows:

$$\left. \begin{aligned} \beta_{a0} &= \frac{1}{[\tanh(m\xi_w) - \tanh(m\xi_c)]} \left[\frac{f_a \sinh^2 \xi_w \cosh \xi_c}{2 \sinh \xi_c} - \frac{f_a \sinh \xi_w \cosh \xi_w}{2} - u_{c,Z} \right], \quad m = 0, \\ \beta_{am} &= \frac{1}{[\tanh(m\xi_w) - \tanh(m\xi_c)]} \left[\frac{f_a \sinh^2 \xi_w \cosh \xi_c e^{-m\xi_c}}{\sinh \xi_c \cosh(m\xi_c)} - \frac{f_a \sinh \xi_w \cosh \xi_w e^{-m\xi_w}}{\cosh(m\xi_w)} \right], \quad m \geq 1. \end{aligned} \right\} \tag{A8}$$

And, therefore, α_{am} can be calculated accordingly.

Finally, the solution (i.e. the particular + homogeneous solution) for the annular fluid velocity field can be written as

$$u_{a,Z} = \frac{f_a \sinh^2 \xi_w \cosh \xi}{2(\cosh \xi - \cos \phi)} + \alpha_{a00} + \beta_{a00} + \sum_{m=1}^{\infty} [\alpha_{am} \cosh(m\xi) + \beta_{am} \sinh(m\xi)] \cos m\phi, \tag{A9}$$

where

$$\alpha_{a00} = \lim_{m \rightarrow 0} (\alpha_{a0} \cosh(m\xi)) = \frac{\xi_w}{\xi_c - \xi_w} \left[\frac{f_a \sinh^2 \xi_w \cosh \xi_c}{2 \sinh \xi_c} - \frac{f_a \sinh \xi_w \cosh \xi_w}{2} - u_{c,Z} \right] - \frac{f_a \sinh \xi_w \cosh \xi_w}{2}, \tag{A10}$$

$$\beta_{a00} = \lim_{m \rightarrow 0} (\beta_{a0} \sinh(m\xi)) = -\frac{\xi}{\xi_c - \xi_w} \left[\frac{f_a \sinh^2 \xi_w \cosh \xi_c}{2 \sinh \xi_c} - \frac{f_a \sinh \xi_w \cosh \xi_w}{2} - u_{c,Z} \right]. \tag{A11}$$

In addition, the shear stresses in the annular phase can be found as

$$\tau_{a,\xi Z} = \frac{M}{\hbar} \frac{\partial u_{a,Z}}{\partial \xi} = \frac{M}{\hbar} \left[-\frac{f_a \sinh^2 \xi_w \sinh \xi \cos \phi}{2(\cosh \xi - \cos \phi)^2} \right] - \frac{M}{\hbar} \frac{1}{\xi_c - \xi_w} \left[\frac{f_a \sinh^2 \xi_w \cosh \xi_c}{2 \sinh \xi_c} - \frac{f_a \sinh \xi_w \cosh \xi_w}{2} - u_{c,Z} \right] + \frac{M}{\hbar} \sum_{m=1}^{\infty} m [\alpha_{am} \sinh(m\xi) + \beta_{am} \cosh(m\xi)] \cos(m\phi), \tag{A12}$$

$$\tau_{a,\phi Z} = \frac{M}{\hbar} \frac{\partial u_{a,Z}}{\partial \phi} = \frac{M}{\hbar} \left[-\frac{f_a \sinh^2 \xi_w \cosh \xi \sin \phi}{2(\cosh \xi - \cos \phi)^2} - \sum_{m=1}^{\infty} m [\alpha_{am} \cosh(m\xi) + \beta_{am} \sinh(m\xi)] \sin(m\phi) \right]. \tag{A13}$$

REFERENCES

AKBARI, S. & TAGHAVI, S.M. 2020 Injection of a heavy fluid into a light fluid in a closed-end pipe. *Phys. Fluids* **32** (6), 063302.
 AKBARI, S. & TAGHAVI, S.M. 2021 Fluid experiments on the dump bailing method in the plug and abandonment of oil and gas wells. *J. Petrol. Sci. Engng* **205**, 108920.
 AL KHATIB, M.A.M. & WILSON, S.D.R. 2005 Slow dripping of yield-stress fluids. *J. Fluids Engng* **127** (4), 687–690.
 ALLOUCHE, M., FRIGAARD, I.A. & SONA, G. 2000 Static wall layers in the displacement of two visco-plastic fluids in a plane channel. *J. Fluid Mech.* **424**, 243–277.
 AMIRI, A., ESLAMI, A., MOLLAABBASI, R., LARACHI, F. & TAGHAVI, S.M. 2019 Removal of a yield stress fluid by a heavier Newtonian fluid in a vertical pipe. *J. Non-Newtonian Fluid Mech.* **268**, 81–100.
 ANNA, S.L. & MCKINLEY, G.H. 2001 Elasto-capillary thinning and breakup of model elastic liquids. *J. Rheol.* **45** (1), 115–138.

- AYTOUNA, M., PAREDES, J., SHAHIDZADEH-BONN, N., MOULINET, S., WAGNER, C., AMAROUCHE, Y., EGGERS, J. & BONN, D. 2013 Drop formation in non-Newtonian fluids. *Phys. Rev. Lett.* **110** (3), 034501.
- BAHRANI, S.A., HAMIDOUCHE, S., MOAZZEN, M., SECK, K., DUC, C., MURADOGLU, M., GROTBORG, J.B. & ROMANÒ, F. 2021 Propagation and rupture of elastoviscoplastic liquid plugs in airway reopening model. *J. Non-Newtonian Fluid Mech.* **300**, 104718.
- BALMFORTH, N.J., DUBASH, N. & SLIM, A.C. 2010a Extensional dynamics of viscoplastic filaments: I. Long-wave approximation and the Rayleigh instability. *J. Non-Newtonian Fluid Mech.* **165** (19–20), 1139–1146.
- BALMFORTH, N.J., DUBASH, N. & SLIM, A.C. 2010b Extensional dynamics of viscoplastic filaments: II. Drips and bridges. *J. Non-Newtonian Fluid Mech.* **165** (19–20), 1147–1160.
- BALMFORTH, N.J., FRIGAARD, I.A. & OVARLEZ, G. 2014 Yielding to stress: recent developments in viscoplastic fluid mechanics. *Annu. Rev. Fluid Mech.* **46**, 121–146.
- BALMFORTH, N.J. & HEWITT, I.J. 2013 Viscoplastic sheets and threads. *J. Non-Newtonian Fluid Mech.* **193**, 28–42.
- BONN, D., DENN, M.M., BERTHIER, L., DIVOUX, T. & MANNEVILLE, S. 2017 Yield stress materials in soft condensed matter. *Rev. Mod. Phys.* **89** (3), 035005.
- BOUJLEL, J. & COUSSOT, P. 2013 Measuring the surface tension of yield stress fluids. *Soft Matt.* **9** (25), 5898–5908.
- BRUN, P.T., AUDOLY, B., RIBE, N.M., EAVES, T.S. & LISTER, J.R. 2015 Liquid ropes: a geometrical model for thin viscous jet instabilities. *Phys. Rev. Lett.* **114** (17), 174501.
- CAGGIONI, M., TRAPPE, V. & SPICER, P.T. 2020 Variations of the Herschel–Bulkley exponent reflecting contributions of the viscous continuous phase to the shear rate-dependent stress of soft glassy materials. *J. Rheol.* **64** (2), 413–422.
- CALIMAN, H.M., SOARES, E.J. & THOMPSON, R.L. 2017 An experimental investigation on the Newtonian–Newtonian and viscoplastic–Newtonian displacement in a capillary tube. *J. Non-Newtonian Fluid Mech.* **247**, 207–220.
- CHAN, S.T., VAN BERLO, F.P.A., FAIZI, H.A., MATSUMOTO, A., HAWARD, S.J., ANDERSON, P.D. & SHEN, A.Q. 2021 Torsional fracture of viscoelastic liquid bridges. *Proc. Natl Acad. Sci. USA* **118** (24), e2104790118.
- CHARLES, N., GAZZOLA, M. & MAHADEVAN, L. 2019 Topology, geometry, and mechanics of strongly stretched and twisted filaments: solenoids, plectonemes, and artificial muscle fibers. *Phys. Rev. Lett.* **123** (20), 208003.
- COUSSOT, P. 2014 Yield stress fluid flows: a review of experimental data. *J. Non-Newtonian Fluid Mech.* **211**, 31–49.
- COUSSOT, P. & GAULARD, F. 2005 Gravity flow instability of viscoplastic materials: the ketchup drip. *Phys. Rev. E* **72** (3), 031409.
- DIMAKOPOULOS, Y. & TSAMOPOULOS, J. 2007 Transient displacement of Newtonian and viscoplastic liquids by air in complex tubes. *J. Non-Newtonian Fluid Mech.* **142** (1–3), 162–182.
- DINGKREVE, M., PAREDES, J., DENN, M.M. & BONN, D. 2016 On different ways of measuring the yield stress. *J. Non-Newtonian Fluid Mech.* **238**, 233–241.
- ESLAMI, A., FRIGAARD, I.A. & TAGHAVI, S.M. 2017 Viscoplastic fluid displacement flows in horizontal channels: numerical simulations. *J. Non-Newtonian Fluid Mech.* **249**, 79–96.
- ESLAMI, A. & TAGHAVI, S.M. 2017 Viscous fingering regimes in elasto-visco-plastic fluids. *J. Non-Newtonian Fluid Mech.* **243**, 79–94.
- ESPINOZA, P.J.T., VARGES, P.R., RODRIGUES, E.C., NACCACHE, M.F. & DE SOUZA MENDES, P.R. 2022 Displacement flow of yield stress materials in annular spaces of variable cross section. *J. Petrol. Sci. Engng* **208**, 109614.
- FERNANDES, R.R., ANDRADE, D.E.V., FRANCO, A.T. & NEGRÃO, C.O.R. 2017 The yielding and the linear-to-nonlinear viscoelastic transition of an elastoviscoplastic material. *J. Rheol.* **61** (5), 893–903.
- FREITAS, J.F., SOARES, E.J. & THOMPSON, R.L. 2011 Immiscible Newtonian displacement by a viscoplastic material in a capillary plane channel. *Rheol. Acta* **50** (4), 403–422.
- FRIGAARD, I.A. 2019 Simple yield stress fluids. *Curr. Opin. Colloid Interface Sci.* **43**, 80–93.
- FRIGAARD, I.A. & NOUAR, C. 2005 On the usage of viscosity regularisation methods for visco-plastic fluid flow computation. *J. Non-Newtonian Fluid Mech.* **127** (1), 1–26.
- GEFFRAULT, A., BESSAIRES-BEY, H., ROUSSEL, N. & COUSSOT, P. 2021 Extensional gravity-rheometry (EGR) for yield stress fluids. *J. Rheol.* **65** (5), 887–901.
- GERMAN, G. & BERTOLA, V. 2010 Formation of viscoplastic drops by capillary breakup. *Phys. Fluids* **22** (3), 033101.

- GOLDSTEIN, A., ULLMANN, A. & BRAUNER, N. 2017 Exact solutions of core-annular laminar inclined flows. *Intl J. Multiphase Flow* **93**, 178–204.
- HABIBI, M., DINGKREVE, M., PAREDES, J., DENN, M.M. & BONN, D. 2016 Normal stress measurement in foams and emulsions in the presence of slip. *J. Non-Newtonian Fluid Mech.* **238**, 33–43.
- HABIBI, M., HOSSEINI, S.H., KHATAMI, M.H. & RIBE, N.M. 2014 Liquid supercoiling. *Phys. Fluids* **26** (2), 024101.
- HABIBI, M., MALEKI, M., GOLESTANIAN, R., RIBE, N.M. & BONN, D. 2006 Dynamics of liquid rope coiling. *Phys. Rev. E* **74** (6), 066306.
- HASSANZADEH, H., ESLAMI, A. & TAGHAVI, S.M. 2021a On the role of the viscosity ratio on buoyant miscible jet flows. *Environ. Fluid Mech.* <https://doi.org/10.1007/s10652-021-09817-2>.
- HASSANZADEH, H., ESLAMI, A. & TAGHAVI, S.M. 2021b Positively buoyant jets: semiturbulent to fully turbulent regimes. *Phys. Rev. Fluids* **6** (5), 054501.
- HU, Y., BIAN, S., GROTBORG, J., FILOCHE, M., WHITE, J., TAKAYAMA, S. & GROTBORG, J.B. 2015 A microfluidic model to study fluid dynamics of mucus plug rupture in small lung airways. *Biomicrofluidics* **9** (4), 044119.
- HYUN, K., WILHELM, M., KLEIN, C.O., CHO, K.S., NAM, J.G., AHN, K.H., LEE, S.J., EWOLDT, R.H. & MCKINLEY, G.H. 2011 A review of nonlinear oscillatory shear tests: analysis and application of large amplitude oscillatory shear (LAOS). *Prog. Polym. Sci.* **36** (12), 1697–1753.
- JALAAL, M. 2016 Controlled spreading of complex droplets. PhD thesis, University of British Columbia.
- JALAAL, M., BALMFORTH, N.J. & STOEBER, B. 2015 Slip of spreading viscoplastic droplets. *Langmuir* **31** (44), 12071–12075.
- JALAAL, M., KEMPER, D. & LOHSE, D. 2019 Viscoplastic water entry. *J. Fluid Mech.* **864**, 596–613.
- JALAAL, M., STOEBER, B. & BALMFORTH, N.J. 2021 Spreading of viscoplastic droplets. *J. Fluid Mech.* **914**, A21.
- JAWORSKI, Z., SPYCHAJ, T., STORY, A. & STORY, G. 2021 Carbomer microgels as model yield-stress fluids. *Rev. Chem. Engng.* <https://doi.org/10.1515/revce-2020-0016>.
- JØRGENSEN, L., LE MERRER, M., DELANOË-AYARI, H. & BARENTIN, C. 2015 Yield stress and elasticity influence on surface tension measurements. *Soft Matt.* **11** (25), 5111–5121.
- KARYAPPA, R., OHNO, A. & HASHIMOTO, M. 2019 Immersion precipitation 3D printing (ip 3DP). *Mater. Horiz.* **6** (9), 1834–1844.
- KHALIFEH, M. & SAASEN, A. 2020 *Introduction to Permanent Plug and Abandonment of Wells*. Springer Nature.
- KORDALIS, A., VARCHANIS, S., IOANNOU, G., DIMAKOPOULOS, Y. & TSAMOPOULOS, J. 2021 Investigation of the extensional properties of elasto-visco-plastic materials in cross-slot geometries. *J. Non-Newtonian Fluid Mech.* **296**, 104627.
- LAWSON, S., LI, X., THAKKAR, H., ROWNAGHI, A.A. & REZAEI, F. 2021 Recent advances in 3D printing of structured materials for adsorption and catalysis applications. *Chem. Rev.* **121** (10), 6246–6291.
- LEAL, L.G. 2007 *Advanced Transport Phenomena: Fluid Mechanics and Convective Transport Processes*. Cambridge University Press.
- MOSCHOPOULOS, P., SYRAKOS, A., DIMAKOPOULOS, Y. & TSAMOPOULOS, J. 2020 Dynamics of viscoplastic filament stretching. *J. Non-Newtonian Fluid Mech.* **284**, 104371.
- NELSON, E.B. & GUILLOT, D. 2006 *Well Cementing*, 2nd edn. Schlumberger Educational Services.
- O'BRYAN, C.S., BRADY-MINÉ, A., TESSMANN, C.J., SPOTZ, A.M. & ANGELINI, T.E. 2021 Capillary forces drive buckling, plastic deformation, and break-up of 3D printed beams. *Soft Matt.* **17** (14), 3886–3894.
- OVARLEZ, G., BARRAL, Q. & COUSSOT, P. 2010 Three-dimensional jamming and flows of soft glassy materials. *Nat. Mater.* **9** (2), 115–119.
- PAN, K., PHANI, A.S. & GREEN, S. 2020 Periodic folding of a falling viscoelastic sheet. *Phys. Rev. E* **101** (1), 013002.
- PEREIRA, A., HACHEM, E. & VALETTE, R. 2020 Inertia-dominated coiling instabilities of power-law fluids. *J. Non-Newtonian Fluid Mech.* **282**, 104321.
- PEREIRA, A., LARCHER, A., HACHEM, E. & VALETTE, R. 2019 Capillary, viscous, and geometrical effects on the buckling of power-law fluid filaments under compression stresses. *Comput. Fluids* **190**, 514–519.
- RAHMANI, Y., HABIBI, M., JAVADI, A. & BONN, D. 2011 Coiling of yield stress fluids. *Phys. Rev. E* **83** (5), 056327.
- RAHMANI, H. & TAGHAVI, S.M. 2020 Linear stability of plane Poiseuille flow of a Bingham fluid in a channel with the presence of wall slip. *J. Non-Newtonian Fluid Mech.* **282**, 104316.
- RASSCHAERT, F., TALANSIER, E., BLÉSÈS, D., MAGNIN, A. & LAMBERT, M. 2018 Packaging of yield stress fluids: flow patterns. *AIChE J.* **64** (3), 1117–1126.

- RIBE, N.M. 2001 Bending and stretching of thin viscous sheets. *J. Fluid Mech.* **433**, 135–160.
- RIBE, N.M. 2003 Periodic folding of viscous sheets. *Phys. Rev. E* **68** (3), 036305.
- RIBE, N.M. 2004 Coiling of viscous jets. *Proc. R. Soc. Lond. Ser. A: Math. Phys. Engng Sci.* **460** (2051), 3223–3239.
- RIBE, N.M. 2017 Liquid rope coiling: a synoptic view. *J. Fluid Mech.* **812**, R2.
- RIBE, N.M., HABIBI, M. & BONN, D. 2012 Liquid rope coiling. *Annu. Rev. Fluid Mech.* **44**, 249–266.
- ROBERTS, G.P. & BARNES, H.A. 2001 New measurements of the flow-curves for Carbopol dispersions without slip artefacts. *Rheol. Acta* **40** (5), 499–503.
- SICA, L.U.R., DE SOUZA MENDES, P.R. & THOMPSON, R.L. 2020 Is the von Mises criterion generally applicable to soft solids? *Soft Matt.* **16** (32), 7576–7584.
- TAGHAVI, S.M. 2018 A two-layer model for buoyant displacement flows in a channel with wall slip. *J. Fluid Mech.* **852**, 602–640.
- TAGHAVI, S.M., SEON, T., MARTINEZ, D.M. & FRIGAARD, I.A. 2009 Buoyancy-dominated displacement flows in near-horizontal channels: the viscous limit. *J. Fluid Mech.* **639**, 1–35.
- TARCHA, B.A., FORTE, B.P.P., SOARES, E.J. & THOMPSON, R.L. 2015 Critical quantities on the yielding process of waxy crude oils. *Rheol. Acta* **54** (6), 479–499.
- TEICHMAN, J. & MAHADEVAN, L. 2003 The viscous catenary. *J. Fluid Mech.* **478**, 71–80.
- THOMPSON, R.L. & DE SOUZA MENDES, P.R. 2020 Rheological material functions at yielding. *J. Rheol.* **64** (3), 615–624.
- TIAN, J., RIBE, N.M., WU, X. & SHUM, H.C. 2020 Steady and unsteady buckling of viscous capillary jets and liquid bridges. *Phys. Rev. Lett.* **125** (10), 104502.
- TRUDEL, E., BIZHANI, M., ZARE, M. & FRIGAARD, I.A. 2019 Plug and abandonment practices and trends: A british columbia perspective. *J. Petrol. Sci. Engng* **183**, 106417.
- VALETTE, R., HACHEM, E., KHALLOUFI, M., PEREIRA, A.S., MACKLEY, M.R. & BUTLER, S.A. 2019 The effect of viscosity, yield stress, and surface tension on the deformation and breakup profiles of fluid filaments stretched at very high velocities. *J. Non-Newtonian Fluid Mech.* **263**, 130–139.
- WISINGER, C.E., MAYNARD, L.A. & BARONE, J.R. 2019 Bending, curling, and twisting in polymeric bilayers. *Soft Matt.* **15** (22), 4541–4547.
- YEE, H.C., WARMING, R.F. & HARTEN, A. 1985 Implicit total variation diminishing (TVD) schemes for steady-state calculations. *J. Comput. Phys.* **57** (3), 327–360.
- ZHANG, X., FADOU, O., LORENCEAU, E. & COUSSOT, P. 2018 Yielding and flow of soft-jammed systems in elongation. *Phys. Rev. Lett.* **120** (4), 048001.
- ZHANG, H.K., YIN, Y.R., ZHANG, X.M., CHEN, S.C., CHEN, W.X. & HU, G.H. 2021 Numerical simulation of the hydrodynamics of yield stress fluids during dip coating. *J. Non-Newtonian Fluid Mech.* **298**, 104675.